Crustal and uppermost mantle structures imaged by teleseismic *P*-wave traveltime tomography beneath the Southeastern Korean Peninsula: implications for a hydrothermal system controlled by the thermally modified lithosphere

Sungho Lee,[1,2] Jung-Hun Song [iD],[1] Dabeen Heo,[3] Junkee Rhie [iD],[1] Tae-Seob Kang [iD],[3] Eunseo Choi [iD],[2] YoungHee Kim [iD],[1] Kwang-Hee Kim [iD][4] and Jin-Han Ree[5]

[1]*School of Earth and Environmental Sciences, Seoul National University, Seoul 08826, Republic of Korea. E-mail:* wjdgns230@snu.ac.kr
[2]*Center for Earthquake Research and Information, University of Memphis, Memphis TN 38152, USA*
[3]*Division of Earth and Environmental System Science, Pukyong National University, Busan 48513, Republic of Korea*
[4]*Department of Geological Sciences, Pusan National University, Busan 46241, Republic of Korea*
[5]*Department of Earth and Environmental Sciences, Korea University, Seoul 02841, Republic of Korea*

SUMMARY

The southeastern Korean Peninsula (SeKP) has experienced intense deformation owing to subduction and backarc extension at the eastern continental margin of the Eurasian Plate, leading to the formation of complex tectonic structures. Abnormally high surface heat flux, Cenozoic volcanism, signatures of mantle degassing and hydrothermal alteration, and several active fault systems with extensional sedimentary basins have been identified; however, the major driving forces that promote local seismic events and hydrothermal activities remain enigmatic. Here, we constructed 3-D *P*-wave velocity of the crust and upper mantle in the SeKP for the first time using a teleseismic traveltime tomography method and an extensive data set obtained from a dense seismic network. Our model revealed three distinct velocity patterns at different depths: (1) in the upper crust (depth ∼0–10 km), a low-velocity anomaly beneath the Cenozoic sedimentary basin exhibiting a prominent lateral velocity contrasts with higher velocities in the Cretaceous sedimentary and plutonic rocks; (2) a N–S trending low-velocity anomaly extending from the lower crust to the uppermost mantle (depth ∼20–35 km) beneath the major active fault systems interpreted as a thermally or mechanically weakened structure that could transfer high surface heat flux and transport mantle-driven gases and (3) a low-velocity anomaly adjacent to the Cenozoic basin in the upper mantle at depths of 35–55 km interpreted as the higher temperature upper mantle. Via a series of geodynamic simulations, we demonstrated that the extensional deformation at the eastern continental margin during the Early to Middle Miocene locally enhanced the temperature of the crust and upper mantle beneath the SeKP. We propose that a hydrothermal system, resulting from the thermally modified lithosphere of the continental margin, has contributed to the enhanced local seismicity and geothermal activities observed in the SeKP region.

Key words: Numerical modelling; Hydrothermal system; Continental margins: convergent; Crustal structure; Teleseismic traveltime tomography; Southeastern Korean Peninsula.

1 INTRODUCTION

The southeastern Korean Peninsula (SeKP) includes distinct geological and tectonic features developed by multiple deformational events at the eastern continental margin of the Eurasian Plate (Fig. 1a). This region overlies the Gyeongsang Basin (Fig. 1a), which is a continental arc-back-arc basin formed in the Cretaceous

period (Chough & Sohn 2010). Tectonic deformations in the SeKP were majorly controlled by the subduction of the palaeo-Pacific (Izanagi) and Pacific plates and backarc opening in the East Sea (Sea of Japan; Chough & Sohn 2010). Several pull-apart basins and strike-slip faults (e.g. Yangsan and Ulsan Faults) were formed during the Cretaceous and Cenozoic periods (Figs 1b and c; Tamaki *et al.* 1992; Jolivet *et al* 1994; Chough *et al.* 2000; Taira 2001;
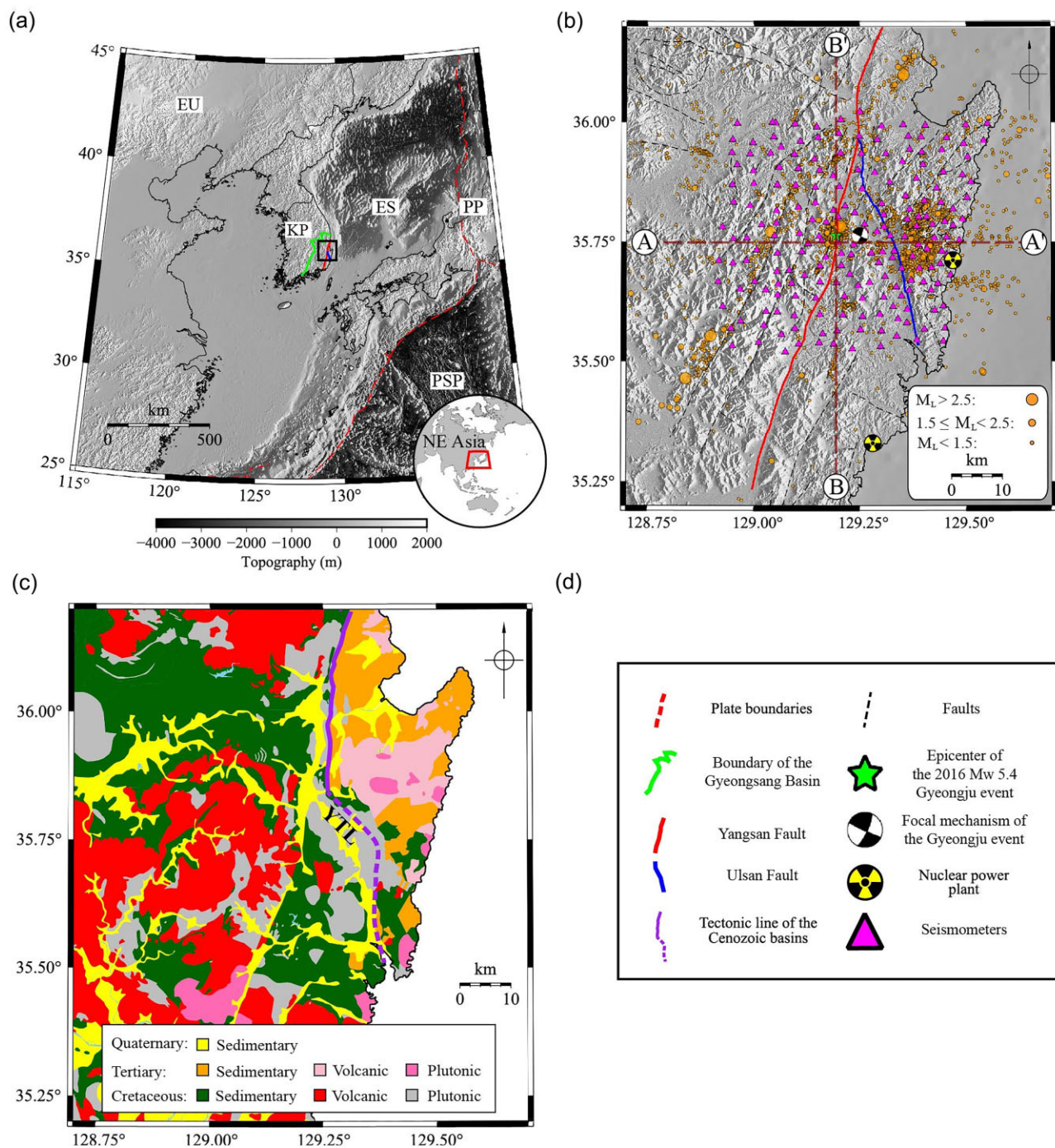
Figure 1. Maps of (a) northeast Asia, (b) the southeastern Korean Peninsula (SeKP) with seismicity since 2019 (Heo *et al.* 2023), (c) geology of the SeKP and (d) legend for panels (a–c). A black rectangular box in (a) shows the map boundary of Figs 1(b) and (c). Plate boundaries depicted by red dashed lines in (a) are from Bird *et al.* (2003). In panel (b), dashed brown lines in (b) indicate the location of vertical profiles shown in Fig. 10, and yellow circles indicate seismic events. ES, East Sea (Sea of Japan); EU, Eurasian Plate; KP, Korean Peninsula; PSP, Philippine Sea Plate and PP, Pacific Plate.

Chough & Sohn 2010). The subduction of the Pacific plate caused the NW–SE trending compressive stress in the late Cretaceous, which was subsequently changed to the NE–SW compression when the Pacific Plate subduction was directed to the west, resulting in crustal thinning of the East Sea during the late Palaeogene (Cheon *et al.* 2019). The opening of the East Sea began at ∼25 Ma with normal faulting, forming the Miocene basins in the eastern SeKP (Son *et al.* 2015). The opening ceased at ∼16 Ma due to the subduction of the Philippine Sea Plate, and compression appeared in the

faults and basins (Choi *et al.* 2015). Previous studies found signatures of hydrothermal alteration (Koh *et al.* 2000; Song *et al.* 2017), groundwater containing mantle-derived gases (Lee *et al.* 2019) and abnormally high surface heat flux (>90 mW m^{-2}; Kim & Lee 2007; Lee *et al.* 2010) adjacent to the fault systems, which are indicative of locally high geothermal gradients due to hydrothermal activity affected by Cenozoic tectonic events (Lee *et al.* 2019).

Several active fault systems are situated in the SeKP (Fig. 1b), and a number of strike-slip faults with distinct seismicity are close

(distance <50 km) to heavily populated city areas (e.g. Busan, Ulsan, Pohang and Gyeongju), nuclear power plants of thousands of Gigawatt hours and national industrial facilities. Among several faults, the Yangsan Fault System in the SeKP, which is an inter-related system of the NNE–SSW trending Yangsan Fault and its splay faults, is the most prominent (Fig. 1b; Kim *et al.* 2016). This fault system is a dominantly right-lateral strike-slip fault with a continuous trace ∼200 km long (Kyung & Lee 2006). The risks associated with the Yangsan Fault have elicited a specific focus on the area since the occurrence of the 2016 M_w 5.4 earthquake; based on instrument-recorded activity since 1978, this earthquake is the largest event in the SeKP (Kim *et al.* 2016; Fig. 1b). In addition, historical records from AD 2 to 1989 indicate several seismic events in the Gyeongsang Basin (>500 events) with at least 126 earthquakes adjacent to the Yangsan Fault (Lee & Jin 1991; Kim *et al.* 2016).

Distribution of local seismicity and hydrothermal activity are closely associated with crustal and upper mantle rheology (Lee *et al.* 2019; Collettini *et al.* 2022). Imaging of deep crustal and upper mantle structures can help constrain rheological conditions of the crust and upper mantle (Fichtner *et al.* 2013). However, due to a lack of seismic surveys that imaged detailed 3-D structures, the crust and upper mantle structures in the SeKP were not well understood. Previous studies reported relatively large-scale structural patterns with a length scale greater than ∼50 km across the Korean Peninsula (Kang & Shin 2006; Chang & Baag 2007; Kim *et al.* 2007; Tao *et al.* 2018; Song *et al.* 2020), exhibiting limited spatial and/or depth resolution to depict detailed structures beneath the SeKP. Previous models showed generally low seismic velocities in the upper crust (Kang & Shin 2006; Kim *et al.* 2007), with crustal thickness gradually decreasing eastward (from 30 to 25 km; Chang & Baag 2007; Lee *et al.* 2016), and a thinner lithosphere (<70 km; Song *et al.* 2020).

Seismic tomography based on a relative traveltime data set of teleseismic body waves has been used to image multiscale crust and upper mantle structures (Aki *et al.* 1977; Rawlinson *et al.* 2006; Rawlinson & Kennett 2008; Schmandt & Lin 2014; Papaleo *et al.* 2017; Zhao 2021). This method has been applied to construct detailed 3-D seismic velocity models beneath a local seismic network while less biased by errors in the event information or velocity heterogeneities outside of modelled space by exploiting individual rays from a common event sharing the same path outside of the region of interest and sampling velocity variations inside the modelled space (Aki *et al.* 1977; Lévêque & Masson 1999; Thurber 2003). The tomographic results have diverse applications in understanding the crustal and upper mantle properties (Mooney *et al.* 2012; Lee *et al.* 2022), volcanism and long-term geological processes (Song *et al.* 2020). However, as teleseismic rays have subvertical trajectories, the vertical velocity contrasts are not as well-constrained as the lateral velocity variations (Rawlinson *et al.* 2006). Therefore, the resolution of the imaged features should be meticulously evaluated by synthetic recovery experiments applying multiscale structures, and the imaged features need to be interpreted based on a comprehensive analysis incorporating prior knowledge of geology and tectonics (Zhao 2021).

In this study, we conducted teleseismic traveltime tomography using data sets from a locally dense network (Fig. 1b) to image detailed 3-D crustal and upper mantle structures in the SeKP. Tomographic inversion was based on the relative traveltime residuals of teleseismic *P* waves measured from high-quality teleseismic waveform data sets recorded by this network. In addition to seismic tomography, we further performed geodynamic simulations to evaluate thermal and compositional conditions of the continental lithosphere affected by the Cenozoic extensional event (Son *et al.* 2015), which were compared with the imaged seismic velocity structures for understanding the evolution of the crust and upper mantle rheology. Together with seismic models and previous geological, geophysical and geochemical observations, we provide reliable insights into the development of the hydrothermal system in the thermally modified continental lithosphere in the SeKP, which could be related to enhanced local seismicity and geothermal activity in this region.

2 DATA AND METHODS

2.1 Seismic events and waveforms

Since September 2019, the Nuclear Safety and Security Commission (NSSC) of South Korea has been operating Gyeongju Hi-density Broadband Seismic Network (GHBSN) consisting of 200 broad-band seismic stations in the SeKP for multiple purposes, one of which is to investigate seismic properties beneath this region (Fig. 1b). The seismic network covers ∼2958 km² [58 (E–W) × 51 (N–S) km²] and has an average inter-station distance of ∼3.5 km (Fig. 1b). All stations feature Nanometrics Trillium compact broad-band sensors in three components with Centaur recorders, and global positioning system clocks that continuously record seismograms at a rate of 200 samples per second. The GHBSN stations collect high-quality teleseismic waveforms, which were used for precisely measuring relative traveltime residuals based on waveform correlation.

We selected 325 teleseismic events between September 2019 to December 2021 with moment magnitudes (M_w) greater than 5.8 at epicentral distances from 30° to 90° from the International Seismological Catalogue, identifying *P*-wave waveforms from the vertical component data. All waveform data were corrected for instrument response and filtered with a two-pole Butterworth bandpass filter with corner frequencies of 0.4–5 Hz. The selection of the filtering band was identical to that used by Papaleo *et al.* (2017), wherein a dense seismic network was used to investigate detailed 3-D crustal structure in the North Anatolian Fault zone employing the same tomographic method. For each event, we identified teleseismic *P* waves around the theoretical arrival time predicted based on the ak135 global reference model (Kennett *et al.* 1995). We calculated signal-to-noise ratios (SNRs) for each waveform, which were defined as $\frac{\text{Signal}_{\text{RMS}}}{\text{Noise}_{\text{RMS}}}$, where the RMS stands for the root mean square calculated for signal (from −2 to 10 s with respect to the *P*-wave arrival) and noise windows (from −15 to −8 s before the *P*-wave arrival). We only selected waveforms showing clear phase arrivals with RMS values >10.0 to be used for calculating relative traveltime residuals.

2.2 Measurement of relative arrival time residuals

We applied the adaptive stacking method to calculate relative arrival time residuals and their uncertainties (Rawlinson & Kennett 2004). This method calculates traveltime residuals by iteratively improving trace alignment based on the relative coherence between each waveform and the reference waveform calculated by stacking all traces. The traces were preliminarily aligned with a theoretical phase arrival time based on the ak135 global reference model (Kennett *et al.* 1995). We set a 12 s time window around direct *P*-wave arrivals for calculating the reference waveform, which was sufficiently wide

to contain the initial phase arrivals (Fig. S1). We allowed a maximum time shift to be ±0.5 s, which was sufficiently large to cover the observed residual times (Fig. S2). To eliminate waveforms that were highly dissimilar to the reference waveform, we calculated cross-correlation coefficients (CCs) between the stacked and individual waveforms and evaluated the degree of waveform similarity between each trace and the stacked waveform using the ratio of CC value of individual waveforms to the average CC value of all waveforms. By removing waveforms with lower ratio values (<0.8), we could only leave waveforms that were highly similar to each other. We also visually checked all waveforms and the results of the stacking procedure to eliminate noisy stations and ensure good-quality picks. For the remaining waveforms, we applied adaptive stacking to determine final traveltime residuals. Finally, the average of the residual times was subtracted from the residual data for each event to obtain the relative residuals. Our data set used for tomographic inversion consists of 37 120 rays from 214 teleseismic earthquakes (Fig. 2a). The uncertainty of each residual arrival time was determined by the similarity between individuals and the reference waveforms and used as a weighting factor for each measurement in tomographic inversion (Rawlinson & Kennett 2004). Examples of calculated residuals are shown in Figs 2(b)–(d).

The inversion of relative arrival-time data to seismic velocity produces relative velocity perturbations with respect to an arbitrary mean velocity at each depth (Aki *et al.* 1977). Consequently, the zero mean of the resultant velocity model is rarely equal to the global mean, and the relatively low- and high-velocity features in the final model may not always correspond to genuinely slow and fast velocities, respectively (e.g. Bastow 2012; Liddell *et al.* 2018). Therefore, care should be taken when interpreting the high- and low-velocity anomalies depicted in the final images by considering the mean absolute velocity conditions of the study area.

2.3 Tomography inversion

Teleseismic traveltime tomography can be performed by inverting the observed data residuals to the velocity perturbations in a local 3-D model. This is achieved by computing the traveltime gradient for the velocity perturbation, which typically involves employing a ray tracing technique to accurately calculate wave propagation in heterogeneous media. The inverse problem is then solved by adjusting the model parameters to satisfy the data subject to regularization constraints. An iterative approach is applied to update the model parameters to account for the non-linear relationship between traveltime and velocity structure (Rawlinson *et al.* 2006).

Tomography inversion was conducted using the teleseismic tomography method developed by Rawlinson *et al.* (2006). This method applies the fast-marching method, which is a grid-based eikonal solver, for accurately calculating traveltimes in the 3-D velocity grids (Rawlinson & Sambridge 2004, 2005). An iterative non-linear process was carried out to invert traveltime data to velocity anomalies based on a subspace inversion method (Kennett *et al.* 1988). We defined the local model volume as a $4° \times 4°$ spherical cap with 91.5 km depth (Fig. 2e), which was wide enough in lateral dimension for all rays to penetrate through the bottom of the domain (Figs 2f and g). Velocity grids had a uniform spacing of $0.033° \times 0.033° \times 3.66$ km inside the model domain (Fig. 2e). The spacing of inversion grids and the maximum depth extent of the model space were determined by resolution tests with synthetic data and inversion results using real data. The initial velocity model was modified from the ak135 global reference model using a crustal

velocity model more relevant to our study area (Kim *et al.* 2011). Variations in Moho depths in the SeKP constrained by previous receiver function studies (Chang & Baag 2007; Lee *et al.* 2016) were considered while calculating the synthetic traveltimes (Rawlinson & Kennett 2008) and were fixed during inversion. We performed 10 iterations during the inversion process, as additional iterations did not significantly improve the data variance and model features. Regularization factors were applied during the inversion procedure (Rawlinson *et al.* 2006). We determined the optimum values of damping (ε) and smoothing (η) as 20 and 10, respectively, based on trade-off curve analyses (Fig. S3).

The reliability of the inverted seismic velocity fields was tested through multiple synthetic tests using input models with checkerboards and specific patterns. All synthetic data were generated using the same source–receiver combination as the observed data set with Gaussian random noise, whose standard deviation was equivalent to 15 per cent (or 30 per cent) of the observed residuals. We conducted conventional checkerboard tests using various checkerboard sizes with diameters of 10.0, 18.6 and 22.2 km and a peak amplitude of ±0.3 km s^{-1}. The sizes of checkerboards were determined based on the scale lengths of the observed anomalies in the solution model. For recovery tests with specific patterns, we applied synthetic structures with spatially separated spike anomalies (Rawlinson *et al.* 2006) or synthetic structures similar to the observed patterns to assess the reliability of the observed structures. For tests with spike anomalies, we applied 11 spatially distributed spikes with a diameter of ~9 km and peak amplitude of ± 0.4 km s^{-1} to evaluate the extent of horizontal and depth smearing in different locations and depths. For tests with synthetic structures, we applied simple block-shaped anomalies that depict the observed patterns at different depths. For all tests, we applied identical model parametrizations (i.e. smoothing and damping) as those applied for the observations. We interpreted the resulting velocity anomalies for the areas showing reliable and robust recovery in the resolution tests.

2.4 Geodynamic modelling

Palaeomagnetic analyses and structural mapping in the SeKP have been used to construct the Miocene tectonic evolution of the basins and fault systems (Son *et al.* 2015). According to this model, the SeKP is composed of two crustal blocks separated by the western boundaries of the Cenozoic basin, which is depicted by the Yeonil tectonic line (YTL) in Fig. 1(c). The block situated east of the Cenozoic tectonic line rotated clockwise due to the backarc opening of the East Sea, while the western block remained unrotated (Fig. 3a). The resultant extension between the blocks formed wedge-shaped basins with igneous activity in 25–16 Ma at the eastern margin of the SeKP. Analysis of structural elements revealed a consistent NNW–SSE tensional stress field for 25–16 Ma (Son *et al.* 2015).

Based on the recent kinematic model, we performed a series of simple numerical simulations using ASPECT 2.5.0-pre (Kronbichler *et al.* 2012; Heister *et al.* 2017; Glerum *et al.* 2018), which is a finite element code for solving the problems pertaining to Earth's convection, to model the extension-driven thermal evolution of the continental lithosphere. The numerical simulations were performed to evaluate the extent of the influence of past extensional events on the temperature and viscosity conditions of the present-day continental lithosphere.

We chose the following set of governing equations under the Boussinesq approximation:

$$-\nabla \cdot \tau(u) + \nabla P = \rho g, \tag{1}$$
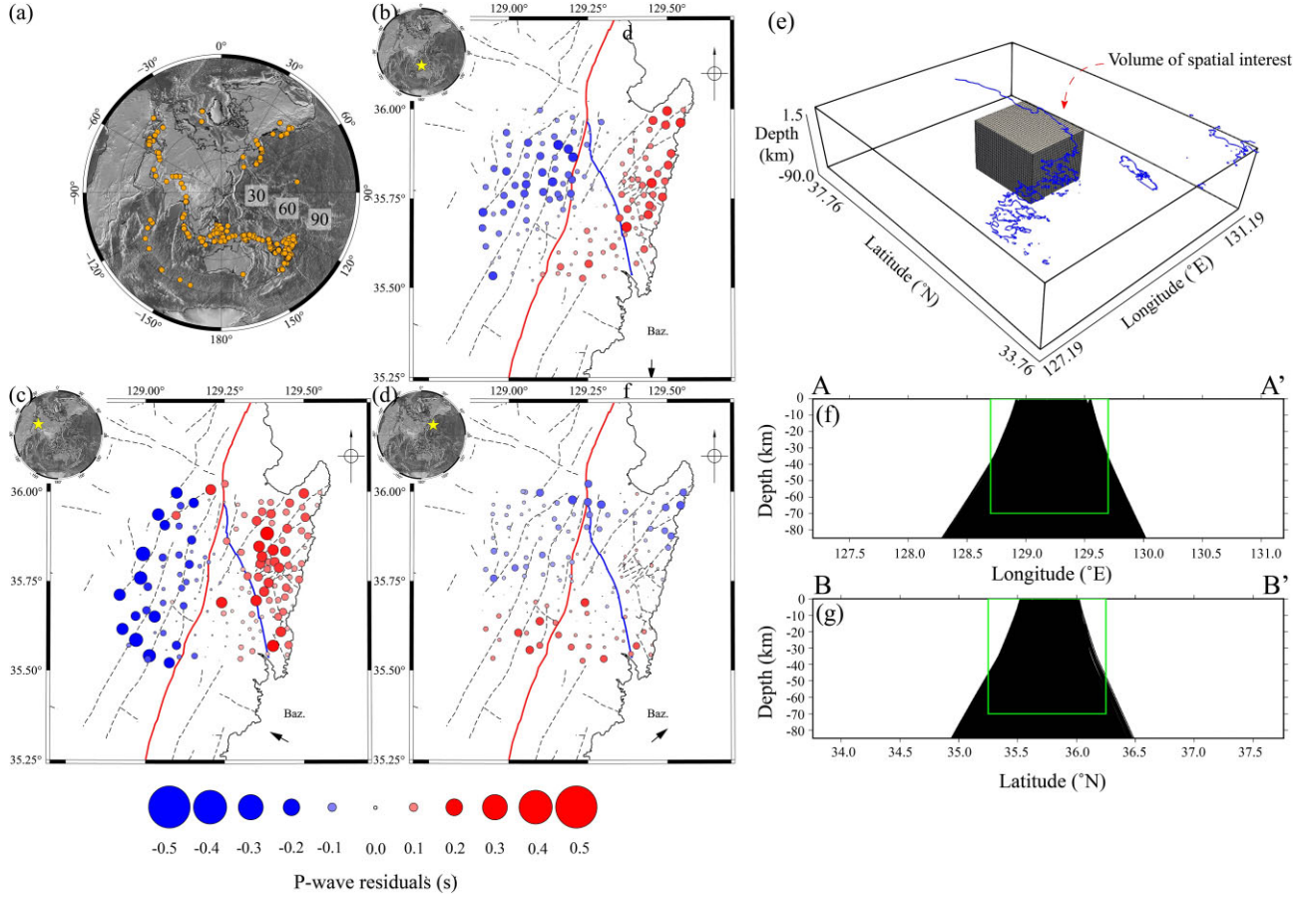
Figure 2. Distribution of events, examples of *P*-wave relative traveltime residual patterns, and numerical domain for tomography inversion. (a) Selected events (orange circles) used in the tomographic inversion. Distribution of relative arrival time residuals for the events from (b) SSE of Sofifi, Indonesia on 14 September 2019 (M_w 5.8), (c) NE of Hashtrud, Iran on 7 November 2019 (M_w 6.0) and (d) SE of Adak, Alaska on 24 November 2019 (M_w 6.3). Red and blue curves indicate Yangsan and Ulsan Faults, respectively, and black-dashed lines indicate other faults. The circular map on the upper left of each panel shows the location of the event, and the black arrow on the lower right indicates average backazimuthal directions (Baz.). (e) Numerical domain for tomography inversion. Teleseismic ray paths projected on the (f) latitudinal axis (A–A' in Fig. 1b) and (g) longitudinal axis (B–B' in Fig. 1b). Blue lines in panel (e) indicate the coastline; the green box in panels (f and g) corresponds to the discretized volume in (e) indicating area of interest for seismic tomography.

$$-\nabla \cdot u = 0, \tag{2}$$

$$\rho C_p \left(\frac{\partial T}{\partial t} + u \cdot \nabla T \right) = k\nabla^2 T + \rho H, \text{ and} \tag{3}$$

$$\frac{\partial C_i}{\partial t} + u \cdot \nabla C_i = q_i, \tag{4}$$

where $\tau(u)$ is the deviatoric stress tensor (Pa), u is the velocity vector (m s^{-1}), P is pressure (Pa), ρ is density (kg m^{-3}), g is the gravity vector (m s^{-2}), C_p is heat capacity (J kg^{-1}K^{-1}), T is temperature (K), t is time (s), k is heat conductivity (W m^{-1} K^{-1}), H is internal heat production (W m^{-3}), C_i is the composition, q_i is the compositional source term, τ is the deviatoric stress tensor, defined as $\tau(u) = 2\eta(\epsilon(u) - \frac{1}{3}(\nabla \cdot u)I)$, ϵ 0 is the strain rate tensor, given as $\epsilon(u) = \frac{1}{2}(\nabla u + (\nabla u)^T)$ and η is the viscosity (Pa·s). Eqs (1)–(4) describe the linear momentum balance, continuity, advection-diffusion of heat energy and advection of the composition field, respectively. Heat capacity and conductivity were assumed to be constant. Diffusion and dislocation creep, with plastic yield, were assumed such that an effective viscosity

was determined as a harmonic average of the viscosities resulting from the two creeping mechanisms and plastic yield. Glerum *et al.* (2018) have provided more details on the formulations of viscoplasticity.

Our model is composed of three layers: the upper crust, lower crust and mantle (Fig. 3b). We assumed an initial thickness of 20 km for the upper crust and 10 km for the lower crust, which are analogous to the average crustal properties of the southern Korean Peninsula (Chang & Baag 2007). The densities of the upper crust, lower crust and mantle were assumed to be 2700, 2900 and 3300 kg m^{-3}, respectively (Turcotte & Schubert 2002). The model parameters were as follows: thermal conductivity = 2.5 W m^{-1} K^{-1}, heat capacity = 750 J kg^{-1} K^{-1}, and volumetric thermal expansivity (α) = 3 × 10^{-5} K^{-1} (Chapman 1986; Turcotte & Schubert 2002). To simulate the rheology of the crust and mantle, we employed laboratory-derived viscous flow laws of the predominant mineral phase associated with each layer (Rybacki & Dresen 2000; Hirth & Kohlstedt 2003; Rutter & Brodie 2004). Specifically, we used wet quartzite for the upper crust, wet anorthite for the lower crust and dry olivine for the mantle. We also assumed an internal friction angle of 30° and cohesion of 20 MPa, which can be weakened by plastic strain. To account for the heterogeneous brittle strength in the
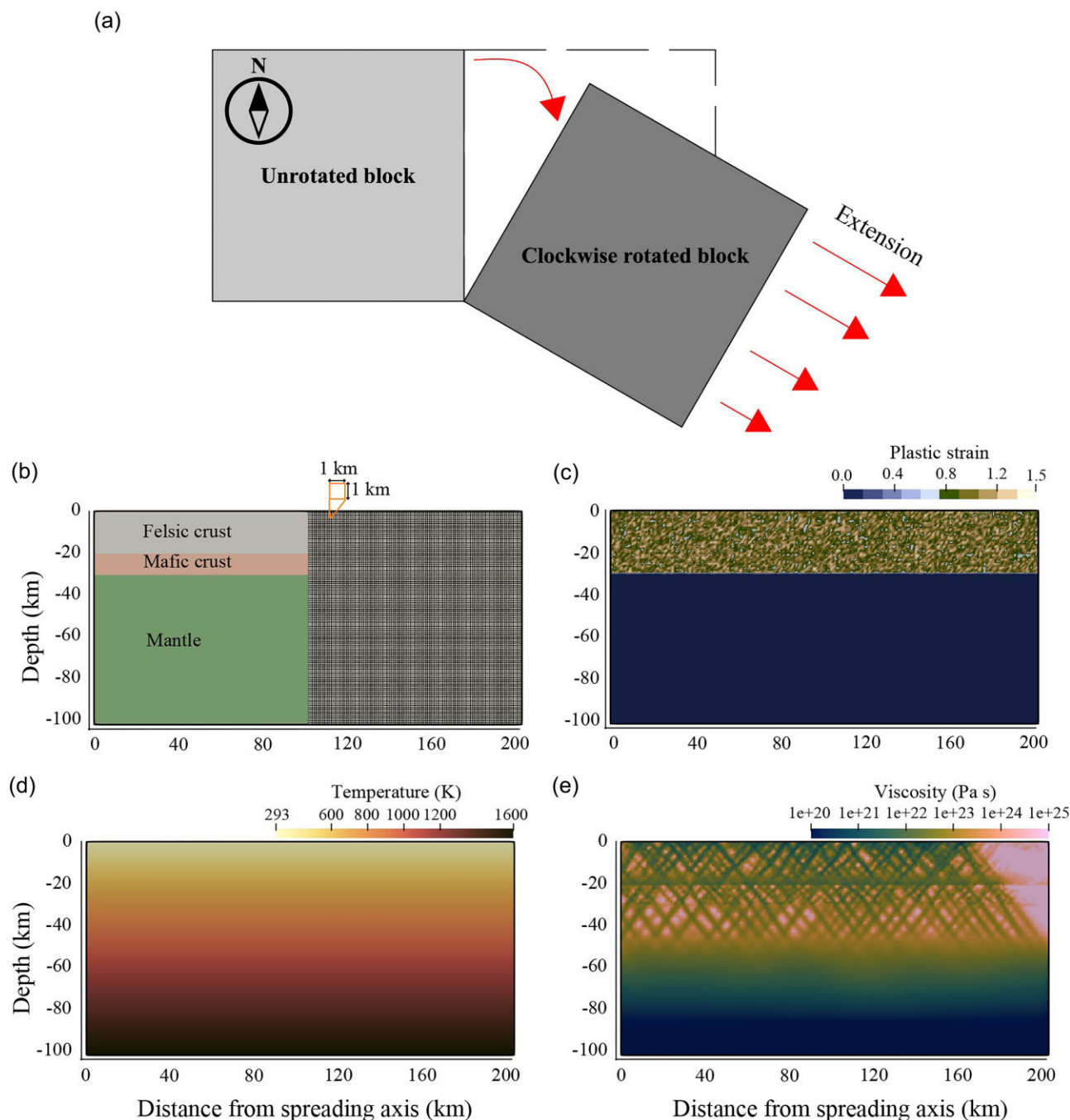
Figure 3. Kinematic model and initial conditions for numerical simulations. (a) The opening mode of the Miocene basins in the SeKP (modified from Son *et al.* 2015). (b) Three-layered model domain (i.e. upper and lower crust and mantle) and computational mesh. Initial (c) plastic strain, (d) temperature and (e) viscosity distributions.

crust, we assumed a random distribution of an initial plastic strain in the range of 0.5–1.5 (Fig. 3c; Naliboff *et al.* 2020). A complete list of the material properties considered in our model is provided in Table S1.

The 2-D model domain covered an area of 20 000 km², with dimensions of 200 and 100 km in the horizontal and vertical directions, respectively. We discretized the model domain into a uniform mesh size (1 km²; Fig. 3b). The left and top boundaries of the domain were set to a free-slip boundary condition, whereas the right boundary had a prescribed boundary condition corresponding to a

half-spreading rate. The remaining bottom boundary was supported by the initial lithostatic pressure to allow the material to move freely in and out. To simulate the divergence of the SeKP crustal blocks, as suggested by the kinematic model (Fig. 3a), we tested half-spreading rates of 1.0, 0.5 and 0.25 cm yr^{-1}, which were labelled as Cases 1–3, respectively. The spreading rates were determined based on ranges of extensional displacements caused by block rotation across the Cenozoic tectonic line (Son *et al.* 2015).

The initial temperature distribution followed the continental geotherm (Chapman 1986; Naliboff & Buiter 2015; Fig. 3d). We

modelled the temperature evolution during the extension and post-extensional period with the temperature fixed at 293 and 1600 K at the top and bottom boundaries, respectively. The extension was assumed to have ceased after the first 9 Myr (25–16 Ma) when the collision of the Philippine Sea Plate with the Japanese Islands occurred (Jolivet *et al.* 1994; Son *et al.* 2015). Tectonic inversion occurred after the collision, and the SeKP is currently under a compressional regime (Heidbach *et al.* 2018). Given that the stress from 16 Ma to the present is relatively minor to overprint the geologic features developed during the extensional period, and that the normal faults formed during the extension still remain active (Choi *et al.* 2015), the right boundary was assumed to be pressure-supported to allow for spontaneous cooling and convection from 16 to 0 Ma.

The primary objective of the present geodynamic simulations is not to accurately predict the present-day temperature distribution but to propose a plausible scenario of relative thermal enhancement resulting from past extensional events, which is expected to cause seismic velocity changes. We evaluated the expected *P*-wave velocity anomalies based on the modelled temperature using the methodologies described in Cammarano *et al.* (2003) and Velocity2Temperature.V1.0 (Lee *et al.* 2022), considering anharmonic and anelastic material properties (Lee *et al.* 2022).

3 RESULTS

3.1 Relative arrival time residuals and tomography results

Figs 2(b)–(d) shows examples of relative arrival time residual maps calculated for teleseismic waveforms aligned by the adaptive stacking procedure (Fig. S1). Later arrivals were observed for stations in the Cenozoic sedimentary basin in the eastern SeKP (Figs 2b and c). This could suggest relatively slow velocity structures located at shallow depths beneath this region. There are also variations in residual patterns depending on event azimuth (Fig. 2d), which indicates that a certain degree of complexity in velocity structures exists at depths beneath the SeKP.

Our final model obtained by the tomography inversion reduced the data variance by 54.06 per cent from 0.0201 to 0.00923 s^2 (from 141.73 to 96.09 ms in RMS; Fig. S2). This reduction is moderate despite the apparent improvement in the observed residuals. This could be due to several unaccounted factors, such as unresolvable shallow or small-scale structures, anisotropy, velocity variations outside of the model space and/or initially small traveltime variances in the modelled region compared to the noise level.

Depth slices through a 3-D *P*-wave tomography model from 5 to 55 km identified three distinct velocity patterns beneath the SeKP (Fig. 4). At a 5 km depth, a low-velocity anomaly ($\leftarrow$200 m s^{-1}; Anomaly 1) was observed east of the Ulsan Fault, showing sharp velocity contrast with a high-velocity anomaly (>200 m s^{-1}) on its west (Fig. 4a). The velocity contrasts between those two anomalies are clearly divided by a Cenozoic tectonic line, which is delineated by the Ulsan Fault and in the northern segment of the Yangsan Fault (Son *et al.* 2015). At a depth of 15 km, the velocity patterns observed at shallower depths became diminished (Fig. 4b) and changed to a N–S trending low-velocity anomaly at 20–35 km depths beneath and around the Yangsan and Ulsan Faults (Anomaly 2; Figs 4c–d). There are lateral variations in the width and strength of Anomaly 2 in both N–S and E–W directions, with its width narrowing southward. The low-velocity structure is segmented into two subregions, one being located beneath the junction of the two faults in the north,

and the other one being located beneath the Yangsan Fault in the south of the seismic array. The velocity patterns changed to E–W trending central low-velocity anomaly at deeper depths (40–55 km; Anomaly 3; Figs 4e–f).

Vertical cross-sections through the 3-D *P*-wave tomography model (Figs 5a–f) clearly depict velocity patterns varying with depth, as shown in the horizontal sections. Structures observed in the horizontal section at 5 km depth are confined at a depth shallower than 12 km (Anomaly 1, Fig. 5c). The depth range of Anomaly 2 is observed to extend from 20 to 35 km, which corresponds to the lower crustal and uppermost mantle depths (Kim *et al.* 2011). The segmented features of Anomaly 2 are merged into the central low-velocity anomaly at deeper depth (40–55 km, Anomaly 3; Fig. 5d).

The series of resolution tests validated that the current ray coverage of our data set (Figs 2f and g) can resolve structures positioned at different depths in the crust and upper mantle (0−12 km, 20−35 km and 35 km below, corresponding to the upper and lower crust, and the upper mantle, respectively) in detail. A series of checkerboard tests revealed that our velocity model generally has good horizontal and vertical resolution beneath the seismic array to depths down to 60 km, except for some smearing at the side edges in the vertical slices (Fig. 6). The tests using the smaller checker size (with a diameter of ∼10 km) showed generally good resolution at shallower depths, indicating that the structures as small as 10 km in both horizontal and vertical directions are resolvable at depths less than ∼35 km. For the larger sizes of checkerboard patterns (with diameters of 18.6 and 22.2 km), the input anomalies were well recovered to deeper depths (∼55–65 km). Synthetic tests with spike anomalies showed that the solution model successfully recovered all the input anomalies, preserving their original polarities and locations without significant merging or smearing between spikes at different positions (Figs 7a–j). Along with synthetic tests with checkerboard and spike anomalies, we conducted tests with structural patterns, which are similar in shape and polarity to the observed features (Anomalies 1–3), to assess the reliability of each anomaly. We first constructed the input structure that has a rectangular shape low-velocity anomaly located at a similar position to Anomaly 1 with a high-velocity anomaly to its west at shallow crustal depths (depth <10 km). The output model showed the original velocity pattern, and the depth extent of the input anomalies was well preserved without significant vertical smearing (Figs S4a-j). Second, we applied synthetic structures used in the previous test added by a N–S directional central low-velocity anomaly at mid- to lower crustal depths, which are similar to Anomalies 1 and 2 (Figs S4k-t). The resultant model showed that the input patterns at different depths were equally well recovered without overlapping. Finally, we tested with input structures of previous models added with an E–W directional central low-velocity anomaly at the upper mantle depths to mimic the observed anomalies (Anomalies 1–3; Figs 7k-t). Similar to the results of the second test, the output model showed that the original shape of individual input patterns at different depths was well recovered in horizontal sections, although vertical smearing may limit resolving the separation of horizontal boundary between closely distributed low-velocity anomalies in the lower crust and upper mantle depth. Furthermore, from synthetic tests with structural input anomalies, all observed features are robust and required structures. The resolving power of our solution model is comparable to that in previous studies wherein detailed imaging of the interior of the crust and uppermost mantle based on a teleseismic data set was conducted (e.g. Papaleo *et al.* 2018; Song *et al.* 2018). Although the amplitudes of input velocity anomalies were degraded, the inversion
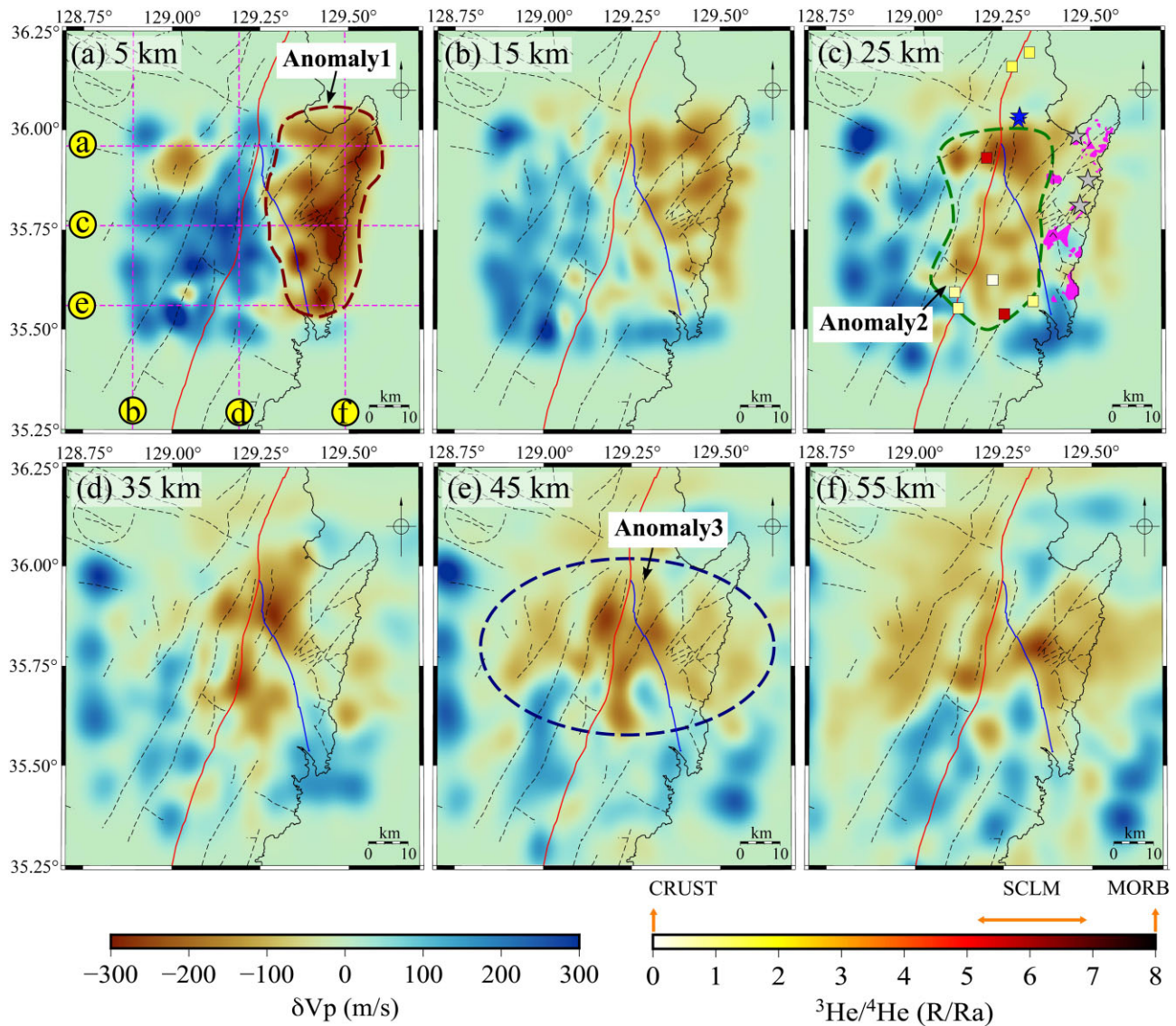
Figure 4. Horizontal slices through the *P*-wave tomography results at depths of (a) 5, (b) 15, (c) 25, (d) 35, (e) 45 and (f) 55 km. Major faults are indicated by solid red (Yangsan Fault) and blue lines (Ulsan Fault), and other faults are indicated by grey dashed lines. Dashed magenta lines in (a) indicate the location of vertical cross-sections in Fig. 5. Dark red-, dark green- and black contour lines indicate mainly interpreted low-velocity anomalies. Panel (c) includes the sample distribution of the ^{3}He/^{4}He ratios (Lee *et al.* 2019), Daljeon (blue stars) and Yeonil (or Eoil) basalts [pink patches indicating their area distribution and grey stars representing the sample sites for geochemical analyses in Choi *et al.* (2013)]. MORB, mid-ocean ridge basalt; SCLM, subcontinental lithospheric mantle.

results with a higher level of noise successfully resolved original input patterns (Figs S5 and S6).

In addition, we also conducted tomographic inversion with station terms, which were inverted together with velocity structures, to evaluate the potential trade-off between traveltime and velocity structures (Rawlinson & Kennett 2008). The results showed that the velocity patterns throughout all depths remained the same, except for some decreases in the amplitude of the anomaly relatively near the surface (<5 km; Fig S7). These results could also indicate that traveltime anomalies raised by unresolvable near-surface structures, if exist, do not significantly affect our main features observed in final velocity model results (Rawlinson & Kennett 2008).

3.2 Numerical simulation of the thermal evolution driven by kinematic extension

Present-day temperature distributions showed a relative increase near the western (axis) boundary compared to that at the initial state, persisting after 16 Myr of cooling for all cases (Figs 8a–i). The elevated temperatures of Cases 1–3 around the spreading axis can be attributed to mantle inflow derived from the bottom during extension (Figs 8a–c). In the model with the fastest spreading rate (Case 1, Fig. 8a), the upward-driven mantle flow injected low-viscosity materials (10^{20} Pa·s) to a depth of ∼10 km, which possibly represents asthenosphere upwelling that displaced the materials initially at a deeper level (∼80 km; Fig. 3e). However, other scenarios
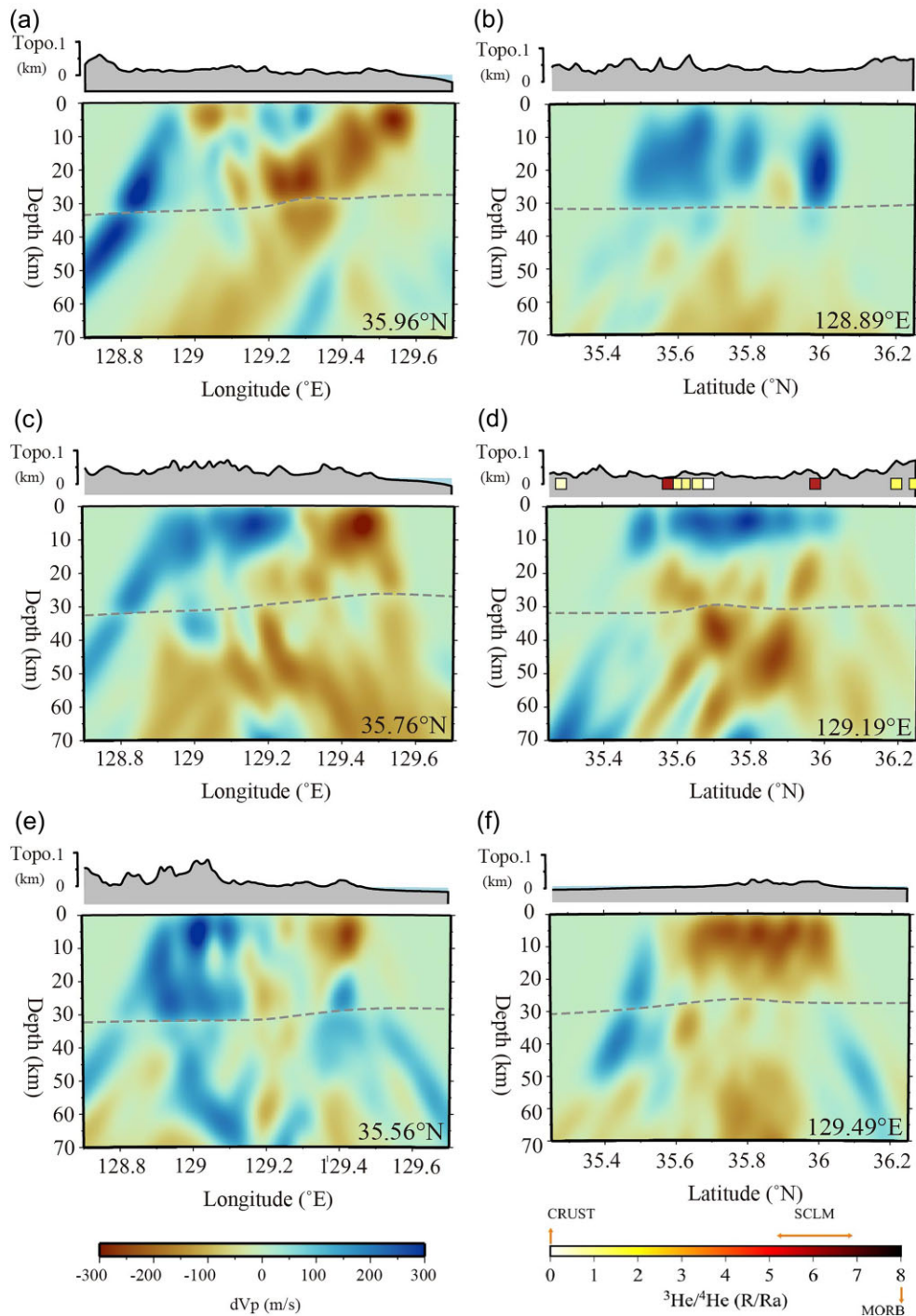
Figure 5. Vertical cross-sections of the *P*-wave tomography results. Profiles in the left-hand column are along (a) 35.96°N, (c) 35.76°N and (e) 35.56°N, and the profiles in the right-hand column are along (b) 128.89°E. (d) 129.19°E and (f) 129.49°E. The grey-dashed lines indicate the Moho depth (Mohorovičić discontinuity) determined by the receiver function analysis of Chang & Baag (2007) and Lee *et al.* (2016). The coloured squares in panel (d) indicate the distribution of the ^{3}He/^{4}He ratios (Lee *et al.* 2019). MORB, mid-ocean ridge basalt; SCLM, subcontinental lithospheric mantle.

showed limited injections of low-viscosity materials into the crustal depth (Figs 8b and c). During the 16 Ma long post-extension period (Figs 8d–f), the relatively high viscosity (>10^{22} Pa·s) layer with weak flow velocities, which corresponds to the lithosphere (crust and upper mantle), cooled from the top via conduction, progressively lowering its temperature. The enhanced thermal conditions (Figs 8g–i) were reflected in the relative *P*-wave velocity reductions (Figs 8j–l). The maximum temperature anomaly and velocity

reductions were observed to be ∼401.8 K and −3.34 per cent, respectively, for Case 1 (Figs 8g and j). The model featuring a high spreading rate (i.e. Case 1) exhibited a laterally extensive *Vp* anomaly, whereas the anomaly in the model with the lowest spreading rate (i.e. Case 3) was only distributed close to the spreading axis; the −0.5 per cent contour extended ∼120–150 km and ∼30–50 km east of the spreading axis for the former and latter, respectively (Figs 8j–l).
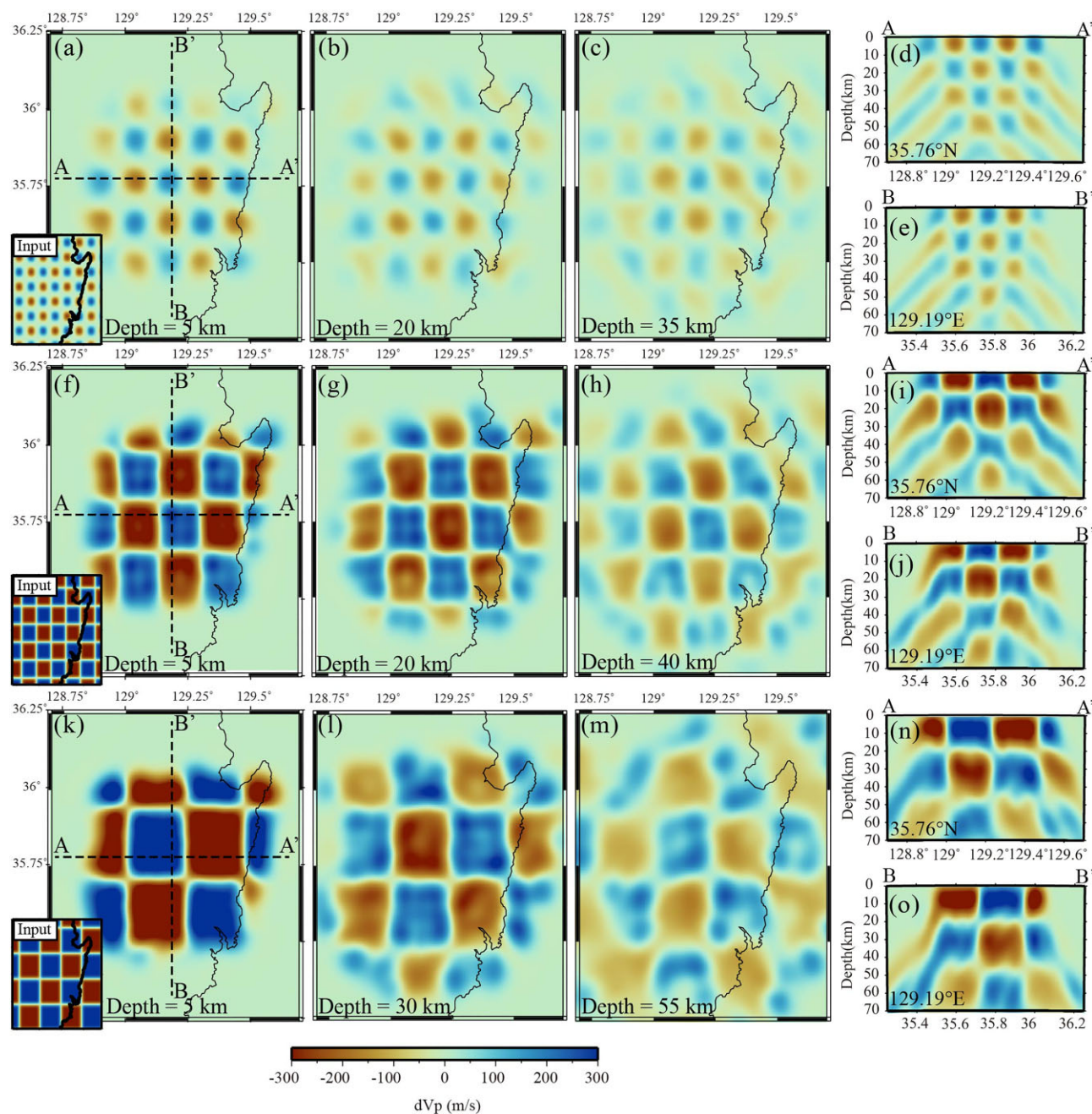
Figure 6. Results of checkerboard resolution tests. (a–e) Test results showing (a–c) horizontal cross-sections at 5, 20 and 35 km depths and (d and e) vertical cross-sections along 35.76°N and 129.18°E using input checker anomalies with a size of ~10 km. (f–j) Same as (a–e) but for input checker anomalies with a size of ~18.6 km. (k–o) Same as (a–e) but for input checker anomalies with a size of ~22.2 km. The input checkerboard patterns are shown in the lower-right-hand panels of horizontal cross-sections at 5 km depth.

4 DISCUSSION

The main observations from our tomography model are summarized as follows: (1) in the upper crust (depth <10 km), low-velocity anomalies beneath the Cenozoic sedimentary basin in the eastern SeKP showing sharp lateral velocity contrasts with higher velocities of Cretaceous sedimentary and igneous rocks to its west, (2) in the lower crust and uppermost mantle (depth ~20–35 km), N–S trending low-velocity anomalies beneath active fault systems and (3) in the upper mantle (depth >35 km), E–W trending low-velocity anomaly that traverses major fault zones and the Cenozoic basin.

Fig. 9 shows a 3-D rendering of our tomographic results depicting volumetric features of the interpreted anomalies. Numerical simulations reflecting the Cenozoic expansion of SeKP have shown that thermal intensification of the crust and upper mantle induced by past expansion deformations can persist to the present day. The seismic images were interpreted by comparing our results with previous geological, geophysical and geochemical observations. Together with numerical simulation results, we discussed the origin of the observed anomalies in association with Cenozoic tectonic deformation at the continental margin of the SeKP.
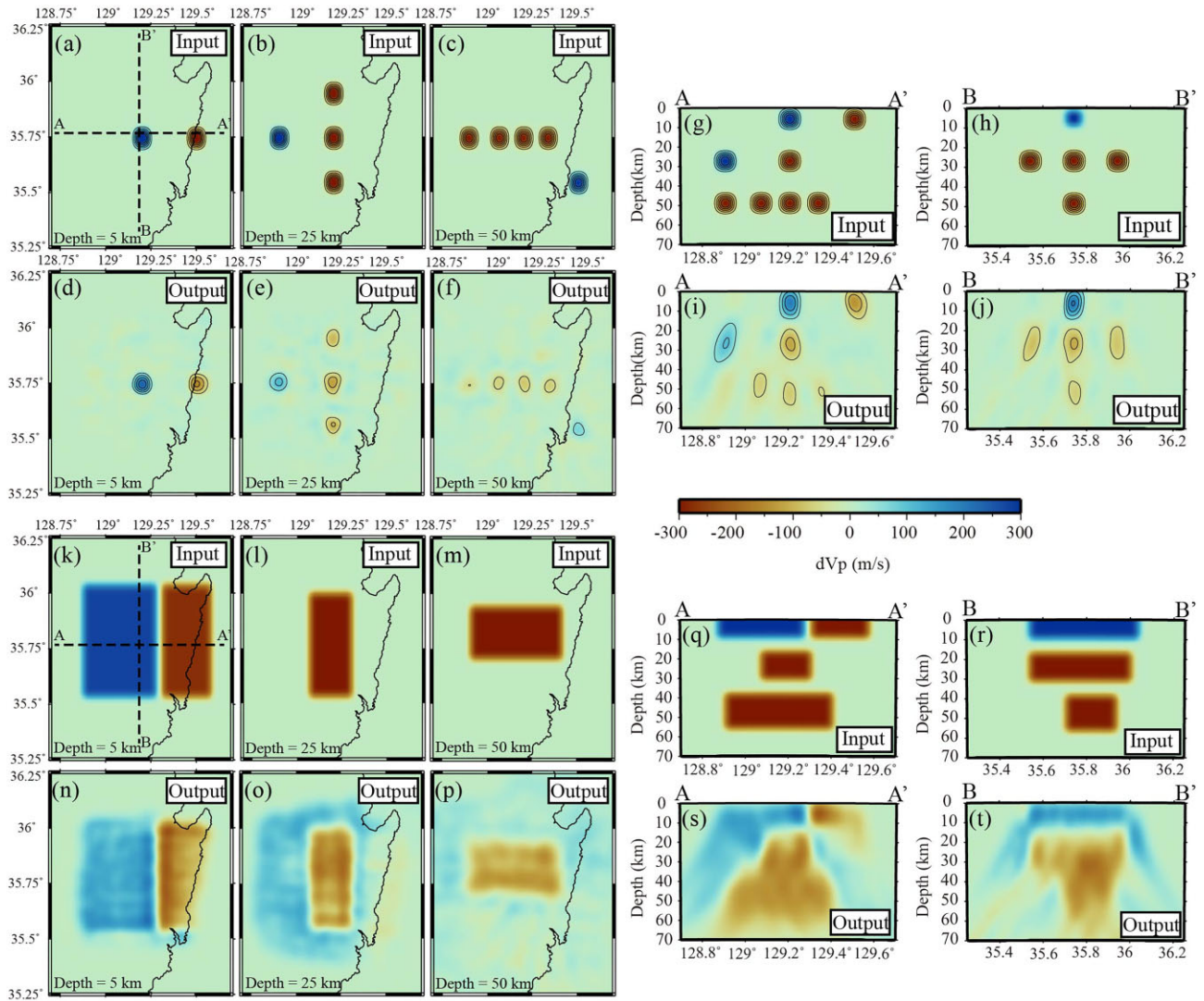
Figure 7. Results of resolution tests using spike anomalies (a–j) and structural patterns (k–f). In each test, input patterns are shown in the upper row. Horizontal cross-sections of the input velocity patterns and the corresponding output results are shown at depths of 5, 25, and 50 km. Vertical cross-sections of the synthetic and corresponding output results are shown along 35.76°N and 129.19°E. Black-dashed contours for the spike resolution test represent ±0.05 km s⁻¹ velocity contours.

4.1 Upper crust low-velocity anomaly beneath sedimentary basin

Depending on the geological context, slow crustal velocities have been attributed to various origins, such as the presence of deep sedimentary basins, lithological variations, elevated temperature, brittle deformation and presence of fluids (e.g. Bourjot & Romanowicz 1992; Miller & Smith 1999; Brocher 2005; Pilia *et al.* 2013; Çubuk-Sabuncu *et al.* 2017; Papaleo *et al.* 2018). The velocity patterns observed in our *P*-wave model in the upper crust (0–10 km depth; Figs 4a and 5c) are comparable to the surface geological features (Fig. 1c). The low-velocity regions (Anomaly 1) are spatially correlated with areas composed of Cenozoic sedimentary (mixed sedimentation environment, that is marine and non-marine; Fig. 1c), while the high-velocity regions are located beneath the Cretaceous sedimentary (nonmarine) or igneous rocks (Chough *et al.* 2000; Sohn & Son 2004; Chough & Sohn 2010; Son *et al.* 2015). The boundaries along which sharp velocity transitions occur closely follow the YTL (Fig. 1c) and the northern part of the Yangsan Fault, which are consistent with the western border limit of local

extensional deformation inferred from structural features (Son *et al.* 2015).

The peak-to-peak velocity contrast between the high- and low-velocity anomalies in the upper crust is ∼400 m s⁻¹ (dln*Vp* of ∼7.5 per cent; Fig. 4). The average *P*-wave velocity in the upper crust of the Gyeongsang Basin has been reported as ∼5.34 km s⁻¹ with a *Vp/Vs* ratio of ∼1.68 (Kim *et al.* 2011). Considering these values as the mean seismic velocity characteristics in our study area, the observed low-velocity anomalies are as low as ∼5.14 km s⁻¹. When compared to the average upper crust velocity of ∼5.6 km s⁻¹ in the southern Korean Peninsula, where basement rocks are predominantly crystalline metamorphic or granitic (Chough *et al.* 2000), the low-velocity anomalies are comparatively slower than the average and similar to those of sedimentary rocks (Brocher 2005). However, the absolute velocity of high-velocity anomalies (∼5.54 km s⁻¹) is comparable to the average upper crustal velocity and represents the characteristics of crystalline rocks. The inferred material properties from seismic velocities are also consistent with surface geology (Fig. 1c).
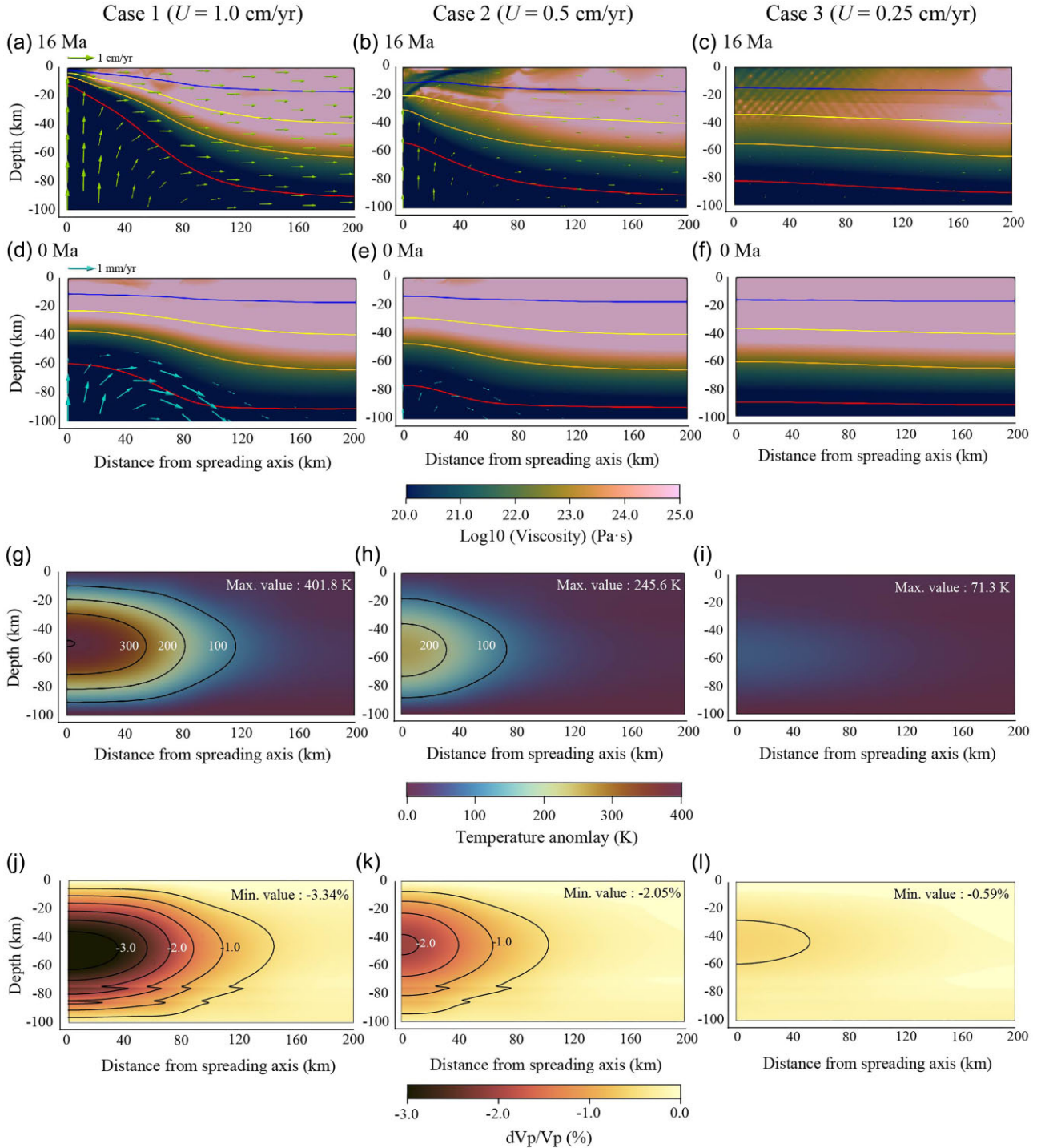
Figure 8. Results of viscosity, velocity, and temperature for different half-spreading rates (*U*). Snapshots at 16 Ma for (a) Case 1 (*U* = 1.0 cm yr^{-1}), (b) Case 2 (*U* = 0.5 cm yr^{-1}) and (c) Case 3 (*U* = 0.25 cm yr^{-1}). Snapshots at 0.0 Ma for (d) Case 1, (e) Case 2 and (f) Case 3. Blue, yellow, orange and red solid contours in panels (a–f) represent temperature lines of 600, 900, 1200 and 1500 K, respectively. Note that the scales of flow velocities (indicated by arrows) are different for different ages. Temperature anomaly (d*T* = *T* − *T*$_{ini}$) at 0.0 Ma for (g) Case 1, (h) Case 2 and (i) Case 3. Inverted *P*-wave velocity anomaly from d*T* at 0.0 Ma for (j) Case 1, (k) Case 2 and (l) Case 3.

The velocity contrasts between different geological units can be explained by seismic wave speeds varied by different rock types (Brocher 2005). The observed lower velocities in sedimentary rocks compared to volcanic or plutonic rocks in our results correspond to generally lower velocity properties of sedimentary rocks than igneous

(volcanic or intrusive) rocks (Brocher 2005). Meanwhile, velocity contrasts between sedimentary basins of different ages could be explained by differences in composition and/or degree of consolidation (Gardner *et al.* 1974). Sediments in the older (Cretaceous) basin likely have experienced more consolidation and cementation than the younger (Cenozoic) basin (Chough & Sohn 2010), which is
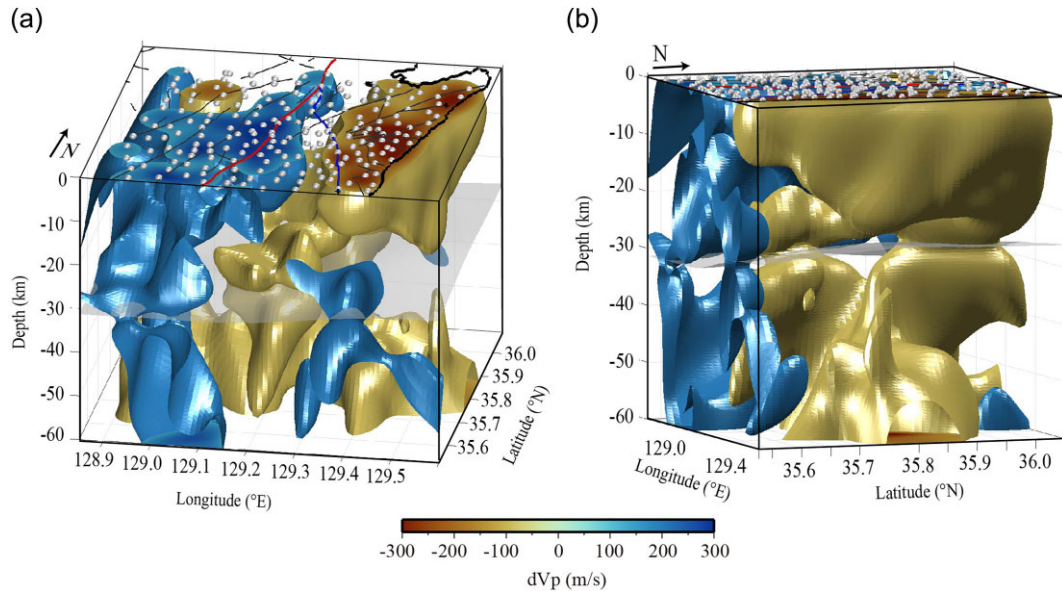
Figure 9. A 3-D plot of the results of *P*-wave tomography. Brown and blue structures represent the -75 m s^{-1} and $+75$ m s^{-1} d*Vp* isosurfaces, respectively. Transparent grey surfaces represent the Moho interface. White circles on the surface represent seismic stations.

supported by a higher density of sampled rocks from the older basin compared to those of the younger basin in the SeKP region (Fig S8). The younger basin includes loose sediments with low elastic modulus and density, which results in lower seismic velocity (Gardner *et al.* 1974). A ∼9-km-thick succession of nonmarine, sedimentary and volcanic deposits accumulated in the Gyeongsang Basin during the Cretaceous (Chough *et al.* 2000; Sohn & Son 2004; Chough & Sohn 2010). The observed sharp lateral velocity contrasts at 0–10 km depths could be associated with velocity contrasts between a thick (>1 km) Miocene sedimentary basin (Sohn *et al.* 2001) and older sedimentary and/or igneous rocks in the Gyeongsang Basin.

4.2 Lower crust and upper mantle low-velocity anomalies beneath active fault systems

We observed distinct N–S trending low-velocity anomalies (Anomaly 2) majorly beneath the active fault systems (Figs 4c and d) in the lower crust and the uppermost mantle depths (∼20–35 km). The velocity anomalies are located along the Yangsan Fault and between the Yangsan and Ulsan Faults. The velocity patterns are distinguished from those observed in the upper crust, indicating that their origins could be different from surface geology.

The velocity patterns in the lower crust and uppermost mantle depths show less association with the general trends in the Moho depth (Fig. 5). On the E–W cross-sections (Figs 5a, c and e), the crustal thickness revealed by a receiver function analysis from a local array in the SeKP (Lee *et al.* 2016) exhibits gradually decreasing trends toward the east from 31 to 25 km without sharp local depth changes. It can be expected that a seismic wave passing through deeper Moho areas arrives later in comparison to shallower Moho as the ray encounters a larger portion of the crust. If the effects from variable Moho depths were significant, the lateral trend of Moho depth in this area would generate slower to faster velocity patterns from west to east. However, such seismic contrasts were not observed in the vertical cross-sections (Figs 5a, c and e), indicating that the observed anomalies are mainly contributed by volumetric structures rather than the variations in Moho depth.

The observed low-velocity anomalies in the lower crust exhibited a maximum velocity reduction of ∼−200 m s^{-1} (dln*Vp* of ∼3.10 per cent). Considering the average lower crustal velocity of ∼6.44 km s^{-1} in the Gyeongsang Basin, the low-velocity anomalies of *Vp* are as slow as ∼6.22 km s^{-1}. This estimate is comparably slower than the lower crustal velocities of the southern Korean Peninsula (6.47–6.66 km s^{-1}; Kim *et al.* 2011, 2017) and the global averages of extensional continental settings (6.4–7.8 km s^{-1}; Christensen & Mooney 1995). At least a local temperature increment of ∼400 K is expected to account for the seismic velocity reduction using the temperature gradient on seismic velocity (Christensen & Mooney 1995). However, such a local high temperature would likely have generated locally prominent surface features, such as high topography or high surface heat flows (Levandowski *et al.* 2014). Owing to the absence of distinct geological features above Anomaly 2, increased temperature cannot be considered as the sole cause of velocity reduction. Instead, the presence of a magma chamber, fluids (Huang & Zhao 2004) or a pre-existing zone of weakness (e.g. localized shear zone; Papaleo *et al.* 2018) has been suggested to explain the presence of seismically slow velocities in the lower crust. In the absence of active volcanoes or recent volcanic activity in the study area, we consider that fluids and/or the presence of shear zones are potential factors contributing to the reduction in lower crustal velocity. Lower crustal low-velocity anomalies with widths ranging from 20 to 180 km have also been observed beneath major strike-slip fault systems and interpreted as effects of local shear zones (Ford *et al.* 2014; Papaleo *et al.* 2018). Various structural observations around the Yangsan Fault System have suggested multiple stages of shearing since the Cretaceous (Kim *et al.* 2022) and can be responsible for the development of the local shear zone beneath the active fault system.

The velocity patterns observed in the upper mantle depths (Anomaly 3) agree with a regional *P*-wave tomography (Fig S9) imaged by Song *et al.* (2020), wherein there is a presence of a low-velocity anomaly elongated in the E–W direction at the upper mantle depths of 40–60 km (Fig S9e and f) whose trends are similar to the Anomaly 3 (Figs 4e and f). Song *et al.* (2020) compared their results with the previous tomography models (see references

therein) and suggested that the observed upper mantle low velocities in the SeKP region are slower than those of the normal mantle, indicating the presence of thermally elevated upper mantle. Meanwhile, the low-velocity anomaly in our model shows rather sharper lateral velocity changes (>1 per cent) across its boundaries than that of the previous model, where a relatively broad low-velocity anomaly was observed across the SeKP.

Considering the generally slower upper mantle in NE Asia compared with the global average ($\sim$−1 per cent in Vp) and the peak-to-peak velocity changes (Anomaly 3) of $\sim$3.5 per cent in our model, the observed reductions in velocity of Anomaly 3 correspond to temperature increments of $\sim$450 K (Karato 1993; Goes *et al.* 2000) with anelastic attenuation in the corresponding depth range ($Qs \sim$ 200) considered (Adenis *et al.* 2017). However, such variations in the composition and grain size (velocity perturbation $\sim$−1 per cent; Cammarano *et al.* 2003; Faul & Jackson 2005) cannot account for velocity changes even when incorporating relatively weak upper mantle anisotropy (<1 per cent) in this region (Kang & Shin 2009; Wei *et al.* 2016). The presence of a small fraction of partial melt (1–2 per cent) can explain the reduction in seismic velocity (Hammond & Humphreys 2000), which has also been suggested in previous tomography studies (Song *et al.* 2020). We suggest that Anomaly 3 reflect weak mantle rheology caused by the presence of partial melt and/or locally higher temperature.

Geodynamic simulation results and physical properties of the crust and upper mantle inferred from Anomalies 2 and 3 suggest that the crust and upper mantle structures beneath the SeKP were thermally enhanced by Cenozoic extension. Structures inherited from the thinned lithosphere caused by past extension persisted through the cooling period ($\sim$16 Ma) after the extension ceased (Fig. 8). Numerical simulations indicate that the elevated temperature is possibly caused by mantle upwelling. The Cenozoic extension event locally thinned the lithosphere, resulting in an influx of hotter asthenospheric material into the relatively shallow upper mantle. Partial melts can be generated in the upper mantle if the temperature of the upwelled mantle exceeds its solidus, depending on compositions and volatile contents (Katz *et al.* 2003; Hirschmann 2006). Assuming a dry peridotite and a potential temperature of 1300–1400 °C (Ball *et al.* 2021), partial melts form at depths of 55–80 km, which are comparable to the inferred depth of mantle melting ($\sim$55 km) from our tomographic results. Two geochemically different groups of basalt have been reported: the 13–15 Ma old alkaline Daljeon basalt (blue stars in Fig. 4c) and the 16–22 Ma old subalkaline Yeonil (or Eoil) basalt (grey stars in Fig. 4c; Choi *et al.* 2013; Shin 2013). Geochemical and isotopic compositions of the volcanic rocks within the Tertiary basins of the SeKP indicate that rift-induced lithospheric thinning and the thermal effect of asthenospheric upwelling could have initiated partial melting of the subcontinental lithospheric mantle (SCLM; Choi *et al.* 2013). The Daljeon basalt exhibits typical characteristics of ocean island basalts and originates from asthenospheric upwelling and lithospheric thinning (Choi *et al.* 2013). Furthermore, Sohn & Son (2004) identified relatively deep-marine sedimentation (>500 m) at $\sim$17 Ma in the Daljeon area, which supports lithospheric thinning or necking beneath this region. This lithospheric thinning was, followed by partial melting and subsidence, according to Airy's isostasy (Brune *et al.* 2014). We note that compared to the lateral extent of Anomalies 2 and 3, Cenozoic basalts are concentrated to the east (Fig. 8c). One plausible explanation for this displacement is that the necking of the lithosphere (and associated crustal thinning) might have been more concentrated beneath the erupted area, which is supported by the presence of an extensional basin with several normal faults

overlapping the erupted region, as reported by Son *et al.* (2015), along with the observation of a shallower Moho depth towards the east (Fig. 5c). This phenomenon could be linked to the non-uniform initial rheological (or lithological) conditions of the crust and lithospheric mantle before the extensional phase (Tetreault & Buiter, 2018), which were not considered in our numerical simulation. Another possible explanation is that even though partial melts were generated in a broader area, as indicated by Anomaly 3, the eruptions might have been concentrated towards the east due to the presence of weaker overlying crusts that are more susceptible to magma injection, unlike the crusts found in the western YTL, which possess a thicker crust with a crystalline basement. To comprehensively assess the suggested scenarios, additional information is required, such as detailed stratigraphy, which helps delineate the spatial extent of basaltic volcanism with the ages of erupted samples. Furthermore, conducting numerical simulations that account for potential non-uniformity in the crust during the pre-extensional stage will help resolve the time-evolving process of basin formation and surface volcanism (Gerya & Burg, 2007).

The present-day Vp anomalies expected from the numerical simulations provide a plausible explanation for expansion of the thermally enhanced structures at greater depths: irrespective of the spreading rate, the lateral extent of the low-velocity anomaly widens with increasing depth, reaching its maximum at $\sim$55 km (Figs 8j–l). This trend is similar to the tomographic results, which show that Anomaly 2 is distributed over a confined area below the N–S trending Cenozoic tectonic line with a lateral extent of <50 km, whereas Anomaly 3 covers a larger area extending laterally in the E–W direction.

4.3 Potential hydrothermal system in the SeKP

The SCLM-derived gas, characterized by a ^{3}He/^{4}He ratio 5.2–7.0 (Gautheron & Moreira 2002; Lee *et al.* 2019) was sampled above Anomaly 2 beneath the major active fault systems (Fig. 10). Based on mantle degassing around the active fault systems in the SeKP region, Lee *et al.* (2019) have suggested that active faults, such as the Yangsan and Ulsan Faults, could be weakened by mantle-derived high-pressure fluids containing volatiles. Occurrence of high strain-induced local shear zones in the lower crust and lithospheric mantle facilitates the migration of deep fluids towards the surface (Lee *et al.* 2019). The southern and northern margins of Anomaly 2 exhibit slower velocities, which are adjacent to areas with higher ^{3}He/^{4}He ratios (>5.5; Figs 4c and 5d) at the surface. These findings could support the model proposing that lithospheric mantle-derived hydrothermal fluids reach the surface via shear zones in the lower crust and brittle upper crust in the SeKP (Lee *et al.* 2019; Fig. 10b). Similar low-velocity anomalies in the lower crust and uppermost mantle have been observed in strike-slip fault systems of other areas where mantle-derived gases have also been observed (Kennedy *et al.* 1997; Fichtner *et al.* 2013; Papaleo *et al.* 2017; Wang *et al.* 2020)

We propose that the presence of low-velocity features in the lower crust and uppermost mantle beneath the SeKP is indicative of structures associated with hydrothermal activities. Previous studies have reported the existence of hydrothermally altered rocks in the SeKP (Koh *et al.* 2000; Song *et al.* 2017), further supporting the development of a hydrothermal system governing the convecting and advecting aqueous- and gas-phase fluids. Fluids within the crust can influence local stress fields and the occurrence of earthquakes (Miller *et al.* 2004; Cappa *et al.* 2009; Geoffroy *et al.* 2022). The
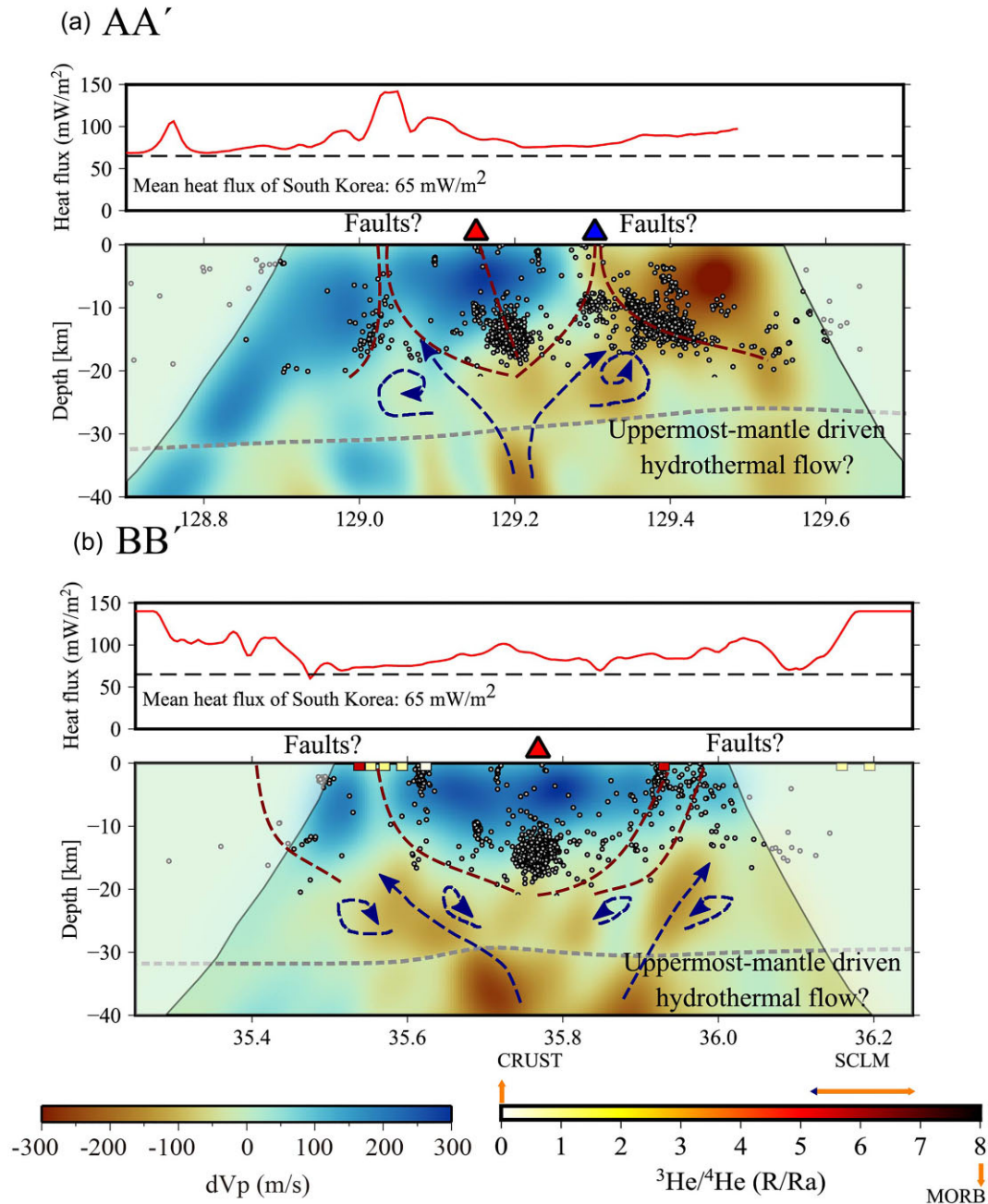
Figure 10. Vertical cross-sections through the 3-D model on (a) AA' and (b) BB' lines along 35.76°N and 129.19°E. The location of vertical cross-sections is shown in Fig. 1(b). Black-dashed line indicating the Moho depth (Mohorovičić discontinuity) is from Chang & Baag (2007). Grey circles indicate seismicity, which is ±0.075° adjacent to the cross-sections. Panel (b) includes the distribution of $^3He/^4He$ ratios (Lee *et al.* 2019). Red and blue triangles indicate the location of Yangsan and Ulsan Faults, respectively. The dashed red lines indicate the deeply extending faults expected from the seismicity, and the dashed blue lines depict the proposed hydrothermal fluid flows. MORB: mid-ocean ridge basalt, SCLM: subcontinental lithospheric mantle.

relatively higher heat flows (75–148 mW m^{-2}; Figs 10 and S10) in the SeKP compared to the mean heat flux of southern Korean Peninsula (∼65 mW m^{-2}) indicate elevated crustal temperatures in the former (Lee *et al.* 2010). High pore pressure and/or high strain rates can extend the depth of brittle failure into the lower crust (Balfour *et al.* 2015). Combined with the elevated $^3He/^4He$ values around the Yangsan Fault indicating the presence of mantle-derived fluids (Lee *et al.* 2019) and the lower crustal properties inferred from Anomaly 2, we propose that the occurrence of seismic events at relatively deeper crustal depths (>15 km) could be partly assisted by

fluids. The earthquakes are concentrated in the velocity-transition areas adjacent to Anomaly 2 (Fig. 10), suggesting that the upper boundaries of Anomaly 2 may represent transitional zones between different rheological and/or chemical structures. Fluid flow from the mantle through the crust, evidenced by the observation of mantle-derived gases at the surface, is also proposed in studies to explain enhanced crustal seismicity (e.g. Gold & Soter 1984; Karlstrom *et al.* 2013). Further analyses of seismic focal mechanisms, crustal rheology, strain rates and more accurate determination of hypocentral depths by 3-D crustal velocity structures (e.g. Jung *et al.* 2022)

may provide insights into the contribution of fluids on local seismic activity in the SeKP.

Hydrothermal systems influenced by a thermally modified lithosphere have been observed at active fault systems in other regions (Roche *et al.* 2019; Eshetu *et al.* 2021). The present characteristics of the continental margin of northeast Asia, including our study area, could exhibit tectonic structures inherited from tectono-magmatic activities associated with Cenozoic continental break-up and opening in the East Sea. We suggest that physical modelling studies can be conducted in the future to evaluate the contributions of hydrothermal activity to seismicity and understand the geodynamic setting of the back-arc opening in northeast Asia. The influence of hydrothermal activity on the seismic activities in the SeKP region has not yet been quantitatively investigated. Song *et al.* (2020) suggested that the lithospheric structures were modified and reworked by thermal erosion along the eastern margin of the Korean Peninsula. Lower velocities compared to our study area were imaged in the northeastern region (Goseong) of the southern Korean Peninsula and the Ulleung volcanic island in the East Sea. Cenozoic basalts with mantle degassing are also observed in Goseong (Kim *et al.* 2006, 2021) and the Ulleung volcanic island (Choi 2021; Lee *et al.* 2021). However, a detailed investigation based on seismic tomography using dense local seismic networks, such as the GHBSN, is absent in these areas. Therefore, a comprehensive characterization of seismic structures can contribute to a better understanding of the geodynamics of northeast Asia during the backarc opening and post-opening periods, as well as their contributions to the tectonic activities along the continental margin.

5 CONCLUSIONS

We obtained detailed 3-D velocity images of the crustal and uppermost mantle structures beneath the active fault systems in the SeKP. We used data sets from a dense local seismic network, which consist of 200 broad-band stations for a period of ∼2 yr. We conducted seismic tomography based on the relative traveltime of the teleseismic *P* waves using the fast-marching teleseismic tomography package. To obtain robust residual times of *P* wave, we used a theoretical phase arrival time from the ak135 global reference model and applied the adaptive stacking method. The proposed 3-D *P*-wave model identified three distinct low-velocity anomalies (Anomalies 1–3) at different depths, which were resolved by a series of resolution tests. Next, we compared our *P*-wave solution model with various geological, geophysical and geochemical observations and a series of geodynamic modelling conducted by ASPECT. Based on our seismic images and supplements, we interpreted the following anomalies: (1) Anomaly 1: the lateral east–west sharp contrast at 0–10 km depth can be associated with the ∼9-km-thick older and more consolidated basin, (2) Anomaly 2: the central low in the N–S directions at 20–35 km depth is probably owing to thermally elevated structures that could be a source for the high-heat flux and SCLM-driven gas and (3) Anomaly 3: the northcentral low in the E–W directions at 35–60 km depth indicate a more thermally enhanced structure possibly correlated with intense tensional deformation to produce partial melt in late Early to Middle Miocene. Our study provides insights into a modified uppermost mantle-driven hydrothermal system possibly related to the seismicity and the tectonic history of this region and proposes a possible future research direction to comprehensively understand the contribution of this hydrothermal system to regional seismicity and the geodynamic

scenario in the eastern continental margin in northeast Asia during and after the Cenozoic backarc opening in East Sea.

SUPPORTING INFORMATION

Supplementary data are available at *GJI* online.

Please note: Oxford University Press is not responsible for the content or functionality of any supporting materials supplied by the authors. Any queries (other than missing material) should be directed to the corresponding author for the paper.

DATA AVAILABILITY

Seismic velocity models, traveltime residuals and ASPECT input files, along with the format description, is available from https://doi.org/10.6084/m9.figshare.20306364.v2 (Lee *et al.* 2022).

AUTHOR CONTRIBUTION

Sungho Lee: conceptualization, data curation, formal analysis, investigation, methodology, software, validation, visualization, writing—original draft, writing—review and editing. Jung-Hun Song: data curation, investigation, methodology, software, supervision, writing—original draft, writing—review and editing. Dabeen Heo: resources, writing—review and editing. Junkee Rhie: funding acquisition, resources, supervision, writing—review and editing. Tae-Seob Kang: Resources, Writing—review and editing. Eunseo Choi: investigation, writing—review and editing. YoungHee Kim: resources, writing—review and editing. Kwang-Hee Kim: resources, writing—review and editing. Jin-Han Ree: resources, writing—review and editing.

REFERENCES

Adenis, A., Debayle, E. & Ricard, Y., 2017. Attenuation tomography of the upper mantle, *Geophys. Res. Lett.,* **44**(15), 7715–7724.

Aki, K., Christoffersson, A. & Husebye, E.S., 1977. Determination of the three-dimensional seismic structure of the lithosphere, *J. geophys. Res.,* **82,** 277–296.

Balfour, N.J., Cummins, P.R., Pilia, S. & Love, D., 2015. Localization of intraplate deformation through fluid-assisted faulting in the lower-crust: the Flinders Ranges, South Australia, *Tectonophysics,* **655,** 97–106.

Ball, P.W., White, N.J., Maclennan, J. & Stephenson, S.N., 2021. Global influence of mantle temperature and plate thickness on intraplate volcanism, *Nat. Comm.,* **12**(1), doi:10.1038/s41467-021-22323-9.

Bastow, I.D., 2012. Relative arrival-time upper-mantle tomography and the elusive background mean, *Geophys. J. Int.,* **190**(2), 1271–1278.

Bird, P., 2003. An updated digital model of plate boundaries, *Geochem. Geophys. Geosys.,* **4**(3), 1–52.

Bourjot, L. & Romanowicz, B., 1992. Crust and upper mantle tomography in Tibet using surface waves, *Geophys. Res. Lett.,* **19**(9), 881–884.

Brocher, T.M., 2005. Empirical relations between elastic wavespeeds and density in the Earth's crust, *Bull. seism. Soc. Am.,* **95**(6), 2081–2092.

Brune, S., Heine, C., Pérez-Gussinyé, M. & Sobolev, S.V., 2014. Rift migration explains continental margin asymmetry and crustal hyper-extension, *Nat. Comm.,* **5**(1), 4014, doi:10.1038/ncomms5014.

Cammarano, F., Goes, S., Vacher, P. & Giardini, D., 2003. Inferring upper-mantle temperatures from seismic velocities, *Phys. Earth planet. Inter.,* **138**(3-4), 197–222.

Cappa, F., Rutqvist, J. & Yamamoto, K., 2009. Modeling crustal deformation and rupture processes related to upwelling of deep CO_2-rich fluids during the 1965–1967 Matsushiro earthquake swarm in Japan, *J. geophys. Res.,* **114**(B10), doi:10.1029/2009jb006398.

Chang, S.-J. & Baag, C.-E., 2007. Moho depth and crustal Vp/Vs variation in southern Korea from teleseismic receiver functions: implication for tectonic affinity between the Korean Peninsula and China, *Bull. seism. Soc. Am.,* **97**(5), 1621–1631.

Chapman, D.S., 1986. Thermal gradients in the continental crust, *Geol. Soc. Spec. Publ.,* **24**(1), 63–70.

Cheon, Y., Cho, H., Ha, S., Kang, H.-C., Kim, J.-S. & Son, M., 2019. Tectonically controlled multiple stages of deformation along the Yangsan Fault Zone, SE Korea, since Late Cretaceous. *J. Asian Earth Sci.,* **170**, 188–207.

Choi, H.-O., Choi, S.H., Lee, D.-C. & Kang, H.-C., 2013. Geochemical evolution of basaltic volcanism within the tertiary basins of southeastern Korea and the opening of the East Sea (Sea of Japan), *J. Volc. Geotherm. Res.,* **249**, 109–122.

Choi, J.-H., Yang, S.-J., Han, S.-R. & Kim, Y.-S., 2015. Fault zone evolution during Cenozoic tectonic inversion in SE, Korea, *J. Asian Earth Sci.,* **98**, 167–177.

Choi, S.H., 2021. Geochemistry and petrogenesis of Quaternary volcanic rocks from Ulleung island, South Korea, *Lithos,* **380–381**, doi:10.1016/j.lithos.2020.105874.

Chough, S.K., Kwon, S.-T., Ree, J.-H. & Choi, D.K., 2000. Tectonic and sedimentary evolution of the Korean peninsula: a review and new view, *Earth Sci. Rev.,* **52**, 175–235.

Chough, S.K. & Sohn, Y.K., 2010. Tectonic and sedimentary evolution of a Cretaceous continental arc-back arc system in the Korean Peninsula: New view, *Earth Sci. Rev.,* **101**, 225–249.

Christensen, N.I. & Mooney, W.D., 1995. Seismic velocity structure and composition of the continental crust: a global view, *J. geophys. Res.,* **100**(B6), 9761–9788.

Collettini, C., Barchi, M.R., De Paola, N., Trippetta, F. & Tinti, E., 2022. Rock and fault rheology explain differences between on fault and distributed seismicity, *Nat. Comm.,* **13**(1), 1–11.

Crameri, F., Shephard, G.E. & Heron, P.J., 2020. The misuse of colour in science communication, *Nat. Comm.,* **11**(1), doi:10.1038/s41467-020-19160-7.

Çubuk-Sabuncu, Y., Taymaz, T. & Fichtner, A., 2017. 3-D crustal velocity structure of western Turkey: constraints from full-waveform tomography, *Phys. Earth planet. Inter.,* **270**, 90–112.

Eshetu, A., Mammo, T. & Tilmann, F., 2021. Imaging the Ethiopian rift region using transdimensional hierarchical seismic noise tomography, *Pure appl. Geophys.,* **178**, 4367–4388.

Faul, U.H. & Jackson, I., 2005. The seismological signature of temperature and grain size variations in the upper mantle, *Earth planet. Sci. Lett.,* **234**(1–2), 119–134.

Fichtner, A., Saygin, E., Taymaz, T., Cupillard, P., Capdeville, Y. & Trampert, J., 2013. The deep structure of the North Anatolian fault zone, *Earth planet. Sci. Lett.,* **373**, 109–117.

Ford, H.A., Fischer, K.M. & Lekic, V., 2014. Localized shear in the deep lithosphere beneath the San Andreas fault system, *Geology,* **42**(4), 295–298.

Gardner, G.H.F., Gardner, L.W. & Gregory, A.R., 1974. Formation velocity and density–the diagnostic basics for stratigraphic traps, *Geophysics,* **39**, 770–780.

Gautheron, C. & Moreira, M., 2002. Helium signature of the subcontinental lithospheric mantle, *Earth planet. Sci. Lett.,* **199**(1–2), 39–47.

Geoffroy, L. et al. 2022. Hydrothermal fluid flow triggered by an earthquake in Iceland, *Commun. Earth Environ.,* **3**(1), 1–9.

Gerya, T.V. & Burg, J.P., 2007. Intrusion of ultramafic magmatic bodies into the continental crust: numerical simulation, *Phys. Earth planet. Inter.,* **160**(2), 124–142.

Glerum, A., Thieulot, C., Fraters, M., Blom, C. & Spakman, W., 2018. Nonlinear viscoplasticity in ASPECT: benchmarking and applications to subduction, *Solid Earth,* **9**(2), 267–294.

Goes, S., Govers, R. & Vacher, A.P., 2000. Shallow mantle temperatures under Europe from P and S wave tomography, *J. geophys. Res.,* **105**(B5), 11 153–11 169.

Gold, T. & Soter, S., 1984. Fluid ascent through the solid lithosphere and its relation to earthquakes, *Pure appl. Geophys.,* **122**, 492–530.

Hammond, W.C. & Humphreys, E.D., 2000. Upper mantle seismic wave velocity: effects of realistic partial melt geometries, *J. geophys. Res.,* **105**(B5), 10 975–10 986.

Heidbach, O. et al. 2018. The World Stress Map database release 2016: crustal stress pattern across scales, *Tectonophysics,* **744**, 484–498.

Heister, T., Dannberg, J., Gassmöller, R. & Bangerth, W., 2017. High accuracy mantle convection simulation through modern numerical methods-II: realistic models and problems, *Geophys. J. Int.,* **210**(2), 833–851.

Heo, D., Kang, T.S., Ree, J.H., Kim, K.H., Rhie, J. & Kim, Y., 2023. The geometrical characteristics of causative faults related to clustered earthquakes in the southeastern Korean Peninsula, in *Proceedings of EGU23: the 25th EGU General Assembly,* held 23–28 April, 2023 in Vienna, Austria and Online. Online at https://egu23.eu/, id. EGU-10900.

Hirschmann, M.M., 2006. Water, melting, and the deep Earth H_2O cycle, *Annu. Rev. Earth planet. Sci.,* **34**, 629–653.

Hirth, G. & Kohlstedf, D., 2003. Rheology of the upper mantle and the mantle wedge: a view from the experimentalists, *Geophys. Monogr. Am. Geophys. Un.,* **138**, 83–106.

Huang, J. & Zhao, D., 2004. Crustal heterogeneity and seismotectonics of the region around Beijing, China, *Tectonophysics,* **385**(1–4), 159–180.

Jolivet, L., Tamaki, K. & Fournier, M., 1994. Japan Sea, opening history and mechanism: a synthesis, *J. geophys. Res.,* **99**, 22 237–22 259.

Jung, Y., Woo, J.U. & Rhie, J., 2022. Enhanced hypocenter determination of the 2017 Pohang earthquake sequence, South Korea, using a 3-D velocity model, *Geosci. J.,* **26**(4), 499–511.

Kang, T.-S & & Shin, J.S., 2006. Surface-wave tomography from ambient seismic noise of accelerograph networks in southern Korea, *Geophys. Res. Lett.,* **33**(17), doi:10.1029/2006gl027044.

Kang, T.-S. & Shin, J.S., 2009. Shear-wave splitting beneath southern Korea and its tectonic implication, *Tectonophysics,* **471**(3–4), 232–239.

Karato, S.I., 1993. Importance of anelasticity in the interpretation of seismic tomography, *Geophys. Res. Lett.,* **20**(15), 1623–1626.

Karlstrom, K.E., Crossey, L.J., Hilton, D.R. & Barry, P.H., 2013. Mantle [3]He and CO_2 degassing in carbonic and geothermal springs of Colorado and implications for neotectonics of the Rocky Mountains, *Geology,* **41**(4), 495–498.

Katz, R.F., Spiegelman, M. & Langmuir, C.H., 2003. A new parameterization of hydrous mantle melting, *Geochem. Geophys. Geosys.,* **4**(9), doi:10.1029/2002GC000433.

Kennedy, B.M. et al. 1997. Mantle fluids in the San Andreas fault system, California, *Science,* **278**(5341), 1278–1281.

Kennett, B.L.N., Engdahl, E.R. & Buland, R., 1995. Constraints on seismic velocities in the Earth from traveltimes, *Geophys. J. Int.,* **122**(1), 108–124.

Kennett, B.L.N., Sambridge, M.S. & Williamson, P.R., 1988. Subspace methods for large inverse problems with multiple parameter classes, *Geophys. J. Int.,* **94**(2), 237–247.

Kim, C.M., Cheon, Y., Lee, T.H., Choi, J.H., Ha, S. & Jeong, J.O., 2022. Long-term weakening processes and short-term seismic slip behavior of an intraplate mature fault zone: a case study of the Yangsan Fault, SE Korea, *J. geophys. Res.,* **127**(4), e2021JB023154, doi:10.1029/2021JB023154.

Kim, H., Lee, H., Hong, J., Song, J.H., Takahata, N. & Sano, Y., 2021. Latent magmatism in non-volcanic areas in South Korea, in *Goldschmidt*, 4-9 July 2021, Virtual.

Kim, H.C. & Lee, Y., 2007. Heat flow in the Republic of Korea, *J. geophys. Res.,* **112**(B5), doi:10.1029/2006jb004266.

Kim, K.H. *et al.* 2006. He-Ar and Nd-Sr isotopic compositions of ultramafic xenoliths and host alkali basalts from the Korean Peninsula, *Geochem. J.,* **39**(4), 341–356.

Kim, K.H., Park, J.H., Park, Y., Hao, T.Y. & Kim, H.J., 2017. Crustal structure beneath the southern Korean Peninsula from local earthquakes, *Geophys. J. Int.,* **209**(2), 969–978.

Kim, K.Y., Lee, J.M., Moon, W., Baag, C.-E., Jung, H. & Hong, M.H., 2007. Crustal structure of the southern Korean peninsula from seismic waves generated by large explosions in 2002 and 2004, *Pure appl. Geophys.,* **164,** 97–113.

Kim, S., Rhie, J. & Kim, G., 2011. Forward waveform modelling procedure for 1-D crustal velocity structure and its application to the southern Korean Peninsula, *Geophys. J. Int.,* **185,** 453–468.

Kim, Y., Rhie, J., Kang, T.-S., Kim, K.-H., Kim, M. & Lee, S.-J., 2016. The 12 September 2016 Gyeongju earthquakes: 1. Observation and remaining questions, *Geosci. J.,* **20**(6), 747–752.

Koh, S., Takagi, T., Kim, M., Naito, K., Hong, S. & Sudo, S., 2000. Geological and geochemical characteristics of the hydrothermal clay alteration in South Korea, *Resour. Geol.,* **50**(4), 229–242.

Kronbichler, M., Heister, T. & Bangerth, W., 2012. High accuracy mantle convection simulation through modern numerical methods, *Geophys. J. Int.,* **191**(1), 12–29.

Kyung, J.B. & Lee, K.H., 2006. Active fault study of the Yangsan fault system and Ulsan fault system, southeastern part of the Korean Peninsula, *J. Korean. Geophys. Soc.,* **9**(3), 219–230.

Lee, D.H., Lee, J.M., Cho, H.-M. & Kang, T.-S., 2016. 3D crustal velocity structure beneath the broadband seismic array in the Gyeongju area of Korea by receiver function analyses, *Tectonophysics,* **689,** 89–106.

Lee, H., Kim, H., Kagoshima, T., Park, J.-O., Takahata, N. & Sano, Y., 2019. Mantle degassing along strike-slip faults in the southeastern Korean Peninsula, *Sci. Rep.,* **9**(1), doi:10.1038/s41598-019-51719-3.

Lee, K. & Jin, Y.G., 1991. Segmentation of the Yangsan Fault System: Geophysical studies on major faults in the Kyeongsang Basin, *J. Geol. Soc. Korea,* **27,** 434–449.

Lee, S., Saxena, A., Song, J.-H., Rhie, J. & Choi, E., 2022. Contributions from lithospheric and upper-mantle heterogeneities to upper crustal seismicity in the Korean Peninsula, *Geophys. J. Int.,* **229,** 1175–1192.

Lee, S. *et al.* 2022. Data used in "crustal and uppermost mantle structures imaged by teleseismic P-wave travel-time tomography beneath the Southeastern Korean Peninsula: implications for a hydrothermal system controlled by the thermally modified lithosphere". Figshare. Dataset., https://doi.org/10.6084/m9.figshare.20306364.v2

Lee, W. *et al.* 2021. Trace element and helium isotope geochemistry of the Cenozoic intraplate volcanism in the East Sea (Sea of Japan): Implications for lithosphere-asthenosphere interaction, *Lithos,* **388–389,** doi:10.1016/j.lithos.2021.106075.

Lee, Y., Park, S., Kim, J., Kim, H.C. & Koo, M.-H., 2010. Geothermal resource assessment in Korea, *Renew. Sust. Ener. Rev.,* **14**(8), 2392–2400.

Levandowski, W., Jones, C.H., Shen, W., Ritzwoller, M.H. & Schulte-Pelkum, V., 2014. Origins of topography in the western US: mapping crustal and upper mantle density variations using a uniform seismic velocity model, *J. geophys. Res.,* **119**(3), 2375–2396.

Lévêque, J.-J. & Masson, F., 1999. From ACH tomographic models to absolute velocity models, *Geophys. J. Int.,* **137**(3), 621–629.

Liddell, M.V., Bastow, I., Rawlinson, N., Darbyshire, F., Gilligan, A. & Watson, E., 2018. Precambrian plate tectonics in northern Hudson Bay: evidence from P and S wave seismic tomography and analysis of source side effects in relative arrival-time data sets, *J. geophys. Res.,* **123**(7), 5690–5709.

Miller, D.S. & Smith, R.B., 1999. P and S velocity structure of the Yellowstone volcanic field from local earthquake and controlled-source tomography, *J. geophys. Res.,* **104**(B7), 15 105–15 121.

Miller, S.A., Collettini, C., Chiaraluce, L., Cocco, M., Barchi, M. & Kaus, B.J.P., 2004. Aftershocks driven by a high-pressure CO_2 source at depth, *Nature,* **427**(6976), 724–727.

Mooney, W.D., Ritsema, J. & Hwang, Y.K., 2012. Crustal seismicity and the earthquake catalog maximum moment magnitude (Mcmax) in stable continental regions (SCRs): correlation with the seismic velocity of the lithosphere, *Earth planet. Sci. Lett.,* **357–358,** 78–83.

Naliboff, J.B. & Buiter, S.J.H., 2015. Rift reactivation and migration during multiphase extension, *Earth planet. Sci. Lett.,* **421,** 58–67.

Naliboff, J.B., Glerum, A., Brune, S., Péron-Pinvidic, G. & Wrona, T., 2020. Development of 3-D rift heterogeneity through fault network evolution, *Geophys. Res. Lett.,* **47**(13), e2019GL086611, doi:10.1029/2019GL086611.

Papaleo, E., Cornwell, D.G. & Rawlinson, N., 2017. Seismic tomography of the North Anatolian Fault: new insights into structural heterogeneity along a continental strike-slip fault, *Geophys. Res. Lett.,* **44**(5), 2186–2193.

Papaleo, E., Cornwell, D.G. & Rawlinson, N., 2018. Constraints on North Anatolian Fault Zone width in the crust and upper mantle from S wave teleseismic tomography, *J. geophys. Res.,* **123**(4), 2908–2922.

Pilia, S., Rawlinson, N., Direen, N.G., Cummins, P.R. & Balfour, N., 2013. Structural controls on localized intraplate deformation and seismicity in Southern Australia: Insights from local earthquake tomography of the Flinders Ranges, *J. geophys. Res.,* **118**(5), 2176–2190.

Rawlinson, N. & Kennett, B.L.N., 2004. Rapid estimation of relative and absolute delay times across a network by adaptive stacking, *Geophys. J. Int.,* **157**(1), 332–340.

Rawlinson, N. & Kennett, B.L.N., 2008. Teleseismic tomography of the upper mantle beneath the southern Lachlan Orogen, Australia, *Phys. Earth planet. Inter.,* **167**(1–2), 84–97.

Rawlinson, N., Reading, A.M. & Kennett, B.L.N., 2006. Lithospheric structure of Tasmania from a novel form of teleseismic tomography, *J. geophys. Res.,* **111**(B2), doi:10.1029/2005jb003803.

Rawlinson, N. & Sambridge, M., 2004. Wave front evolution in strongly heterogeneous layered media using the fast marching method, *Geophys. J. Int.,* **156**(3), 631–647.

Rawlinson, N. & Sambridge, M., 2005. The fast marching method: an effective tool for tomographic imaging and tracking multiple phases in complex layered media, *Explor. Geophys.,* **36**(4), 341–350.

Roche, V., Bouchot, V., Beccaletto, L., Jolivet, L., Guillou-Frottier, L., Tuduri, J., Bozkurt, E., Oguz, K. & Tokay, B., 2019. Structural, lithological, and geodynamic controls on geothermal activity in the Menderes geothermal Province (Western Anatolia, Turkey), *Int. J. Earth Sci.,* **108**(1), 301–328.

Rutter, E. & Brodie, K., 2004. Experimental intracrystalline plastic flow in hotpressed synthetic quartzite prepared from Brazilian quartz crystals, *J. Struct. Geol.,* **26,** 259–270.

Rybacki, E. & Dresen, G., 2000. Dislocation and diffusion creep of synthetic anorthite aggregates, *J. geophys. Res.,* **105,** 26 017–26 036.

Schmandt, B. & Lin, F.C., 2014. P and S wave tomography of the mantle beneath the United States, *Geophys. Res. Lett.,* **41**(18), 6342–6349.

Shin, S.-C., 2013. Revised fission-track ages and chronostratigraphies of the Miocene basin-fill volcanics and basements, SE Korea, *J. Petrol. Soc. Korea,* **22**(2), 83–115.

Sohn, Y.K., Rhee, C.W. & Shon, H., 2001. Revised stratigraphy and reinterpretation of the Miocene Pohang basinfill, SE Korea: sequence development in response to tectonism and eustasy in a back-arc basin margin, *Sedimen. Geol.,* **143**(3–4), 265–285.

Sohn, Y.K. & Son, M., 2004. Synrift stratigraphic geometry in a transfer zone coarse-grained delta complex, Miocene Pohang Basin, SE Korea, *Sedimentology,* **51**(6), 1387–1408.

Son, M., Song, C.W., Kim, M.-C., Cheon, Y., Cho, H. & Sohn, Y.K., 2015. Miocene tectonic evolution of the basins and fault systems, SE Korea: dextral, simple shear during the East Sea (Sea of Japan) opening, *J. Geol. Soc.,* **172**(5), 664–680.

Song, J.-H., Kim, S. & Rhie, J., 2020. Heterogeneous modification and reactivation of a craton margin beneath the Korean Peninsula from teleseismic travel time tomography, *Gondwana Res.,* **81,** 475–489.

Song, J.-H., Kim, S., Rhie, J., Lee, S.H., Kim, Y. & Kang, T.S., 2018. Imaging of lithospheric structure beneath Jeju Volcanic Island by teleseismic traveltime tomography, *J. geophys. Res.,* **123**(8), 6784–6801.

Song, S.J., Choo, C.O., Chang, C.J. & Jang, Y.D., 2017. A microstructural study of the fault gouge in the granite, Yangbuk, Gyeongju, southeastern Korea, with implications for multiple faulting, *Geosci. J.,* **21**(1), 1–19.

Taira, A., 2001. Tectonic evolution of the Japanese island arc system, *Annu. Rev. Earth planet. Sci.,* **29,** 109–134.

Tamaki, K., Suyehoro, K., Allen, J., James, C.I. & Pisciotto, K.A., 1992. Tectonic synthesis and implications of Japan Sea ODP drilling, in *Proceedings of the Ocean Drilling Program, Scientific Results,* Vol. 127–128 (Part 2), eds Tamaki, K. *et al.*, pp. 1333–1348.

Tao, K., Grand, S.P. & Niu, F., 2018. Seismic structure of the upper mantle beneath eastern Asia from full waveform seismic tomography, *Geochem. Geophys. Geosys.,* **19**(8), 2732–2763.

Tetreault, J.L. & Buiter, S.J. H., 2018. The influence of extension rate and crustal rheology on the evolution of passive margins from rifting to break-up, *Tectonophysics,* **746,** 155–172.

Thurber, C.H., 2003. Seismic tomography of the lithosphere with body waves, *Pure appl. Geophys.,* **160**(3), 717–737.

Turcotte, D.L. & Schubert, G., 2002. *Geodynamics,* Cambridge Univ. Press.

Wang, K., Jiang, C., Yang, Y., Schulte-Pelkum, V. & Liu, Q., 2020. Crustal deformation in Southern California constrained by radial anisotropy from ambient noise adjoint tomography, *Geophys. Res. Lett.,* **47**(12), e2020GL088580, doi:10.1029/2020GL088580.

Wei, W., Zhao, D., Xu, J., Zhou, B. & Shi, Y., 2016. Depth variations of P-wave azimuthal anisotropy beneath Mainland China, *Sci. Rep.,* **6**(1), 1–10.

Zhao, D., 2021. Seismic imaging of Northwest Pacific and East Asia: new insight into volcanism, seismogenesis and geodynamics, *Earth Sci. Rev.,* **214,** doi:10.1016/j.earscirev.2021.103507.